Journal of Power Sources 382 (2018) 77–94

Contents lists available at ScienceDirect

Journal of Power Sources

journal homepage: www.elsevier.com/locate/jpowsour

A systematic approach for electrochemical-thermal modelling of a large format lithium-ion battery for electric vehicle application

Elham Hosseinzadeh*, Ronny Genieser, Daniel Worwood, Anup Barai, James Marco, Paul Jennings

WMG, University of Warwick, Coventry CV4 7AL, United Kingdom

HIGHLIGHTS

- A large format pouch cell over a wide range of ambient temperatures is characterised.
- The full parameter-set for the model are provided.
- Power and capacity significantly drop by decreasing the ambient temperature.
- The battery optimal operating range is between 25°C - 35°C.

ARTICLE INFO

Keywords:
Electric vehicle
Electrochemical-thermal model
Large format cells
Lithium-ion battery
Drive cycle

ABSTRACT

A 1D electrochemical-thermal model is developed to characterise the behaviour of a 53 Ah large format pouch cell with $LiNi_xMn_yCo_{1-x-y}O_2$ (NMC) chemistry over a wide range of operating conditions, including: continuous charge (0.5C-2C), continuous discharge (0.5C-5C) and operation of the battery within an electric vehicle (EV) over an urban drive-cycle (WLTP Class 3) and for a high performance EV being driven under track racing conditions. The 1D model of one electrode pair is combined with a 3D thermal model of a cell to capture the temperature distribution at the cell scale. Performance of the model is validated for an ambient temperature range of 5°C–45°C. Results highlight that battery performance is highly dependent on ambient temperature. By decreasing the ambient temperature from 45 °C to 5 °C, the available energy drops by 17.1% and 7.8% under 0.5C and 5C discharge respectively. Moreover, the corresponding power loss is found to be: 5.23% under the race cycle as compared with 7.57% under the WLTP drive cycle. Formulation of the model is supported by a comprehensive set of experiments, for quantifying key parameters and for model validation. The full parameter-set for the model is provided ensuring the model is a valuable resource to underpin further research.

1. Introduction

Lithium ion (Li-ion) batteries play a key role in emerging electric vehicles (EVs) and hybrid electric vehicles (HEVs) due to their high energy and high power density [1]. It has been widely reported that many of the battery characteristics such as cycle life, reliability, cost, and in particular energy and power density are highly affected by the operating temperature [2,3]. The choice of the cell as well as the energy/power requirement of the pack, define the framework for designing the thermal management system (TMS) [4]. The primary function of the TMS is to regulate the battery temperature within the optimum range, typically defined to be between 15 and 35 °C [5,6], and to ensure battery safety and durability [5,6]. Higher temperatures improve the performance of li-ion batteries due to temperature dependency of the electrochemical parameters which result in lower internal resistance. However, higher ambient temperatures are known to accelerate the degradation rate due to increased side reactions within the cell [6,7]. Conversely, low temperatures deteriorate cell performance mainly due to the reduced reaction kinetics resulting a high internal resistance [5,6,8]. The impact of low temperature operation is known to become more severe during periods of high current charging or “fast charging” that may result in the onset of lithium plating [9]. Many studies in recent years have focused on analysing the thermal behaviour of the batteries [10]. For example the impact of geometry and position of the tabs on the temperature gradient of a 10 Ah and 75 Ah has been discussed in Refs. [11,12]. Kim et al. [13] investigated the thermal behaviour of a 14.6 Ah pouch cell under 1C, 3C and 5C at 25°C. Taheri et al. [14] used a 2D electro-thermal approach to develop a

* Corresponding author. Tel.: +44(0)24 7615 1374; fax: +44(0)24 7615 1374.
E-mail address: e.hosseinzadeh@warwick.ac.uk (E. Hosseinzadeh).

https://doi.org/10.1016/j.jpowsour.2018.02.027
Received 21 November 2017; Received in revised form 19 January 2018; Accepted 10 February 2018

Nomenclature

List of symbols

A_{surf}	surface area of the cell (m^2)
A_{tab}	cross sectional area of the tab (m^2)
a_s	reaction surface area
$brugg_n$	Bruggeman porosity exponent
C	Li^+ concentration ($mol\ m^{-3}$)
C_p	heat capacity (J $(kg.\ K)^{-1}$)
D	diffusion coefficient ($m^2\ s^{-1}$)
E_{act}	activation energy
F	Faraday's constant ($C\ mol^{-1}$)
h	heat transfer coefficient ($W/(m^2.\ K)$)
I	current load (A)
I_{pair}	current of a single-pair electrode (A)
i_e	ionic current density ($A\ m^{-2}$)
	electronic current density ($A\ m^{-2}$)
i_0	exchange current density ($A\ m^{-2}$)
j^{Li}	reaction current density ($A\ m^{-2}$)
k	thermal conductivity ($W.\ (m.\ K)^{-1}$)
k_i	reaction rate ($m^{2.5}\ mol^{-0.5} s^{-1}$)
L	thickness of the electrode (μm)
N_{pairs}	number of electrode-pairs
Q	heat generation (W)
q	volumetric heat generation ($W\ m^{-3}$)
q'	the heat flux at the exposed cell surface
R	resistance of the current collector (Ω)
R_c	contact resistance between the current collecting tab and the lead wire (Ω)
R_{uni}	universal gas constant ($J\ mol^{-1}K^{-1}$)
R_{SEI}	resistance of the SEI layer ($\Omega.cm^{-2}$)
r	radial coordinate in spherical particle (μm)
r_p	particle radius (μm)
T	temperature ˚C
t	time (s)
t_{dif}	diffusion time (s)
t_{dis}	discharge time (s)
t_+^0	transference number
$U_{ref,i}$	open circuit potential of the electrodes
U_{OCV}	open circuit voltage of the cell
V_t	terminal voltage
x	local state of charge of the negative electrode
y	local state of charge of the positive electrode

Greek letters

α	symmetry factor
δ_{cell}	capacity of a cell (Ah)
ε	volume fraction
η	overpotential (V)
k_D^{eff}	diffusional conductivity ($S\ m^{-1}$)
σ	electronic conductivity ($S\ m^{-1}$)
κ	ionic conductivity ($S\ m^{-1}$)
ρ	Density ($kg\ m^{-3}$), resistivity (Ω.m)
ϕ	potential (V)
ψ	a general parameter

Subscripts/superscripts

a	anode
amb	ambient
c	cathode
cc	current collector
e	electrolyte
eff	effective
elec	electronic
f	filler
irr	irreversible
neg	negative
pos	positive
r	reaction
rev	reversible
s	solid
sep	separator
surf	surface
x	direction through the cell thickness
y	direction along the cell width
z	direction along the cell height

Terms and abbreviation

Al	Aluminium
Cu	Copper
exp	experimental
OCV	open circuit voltage
sim	simulation
SOC	state of charge

reliable model for a 20 Ah NMC prismatic cell. Wu at al. [15] extended their research, combining a 2D electro-thermal with a 3D thermal model and applied it for a 25 Ah pouch cell. They discuss the tab heat generation as the main source for the temperature non-uniformity throughout the battery. Samba et al. [16] developed a 2D thermal model of a 45 Ah cell considering radiation effects, and detailed tab heat generation. Murashko at al. [17] coupled an equivalent electrical circuit with a 3D thermal model and validated their model against experimental data for a 60 Ah pouch cell at 25°*C* ambient temperature for a 1C, 3C and 5C current discharge. Bazinski at al. [18] developed an analytical model to predict the heat generation of a 14.5 Ah LFP cell under different discharge rates.

Even though the topic of thermal modelling of li-on batteries has been broadly investigated, relatively few researchers within the literature have investigated the impact of ambient temperature over a wide range and most of them are limited to 25°*C* ambient temperature. In addition, simple lumped parameter models, such as those presented in Refs. [19,20], cannot provide sufficient details regarding power/capacity loss under different drive cycles/ambient conditions. To capture it, higher fidelity models, such as electrochemical models are required. Examples of electrochemical-thermal models validated at 25°*C* can be seen in Ref. [15] for a 2.3 Ah LFP cylindrical 26650 type cell operating up to 10C, a 10 Ah cylindrical LFP (a commercial type 38120) cell operating up to 2C [21], a 3D model of 10 Ah LFP pouch cell [22], a 15.7 Ah LiMn2O4/graphite pouch cell operating up to 5C [23,24] and a 3D thermal-electrochemical model for a single layer 45 Ah LFP pouch cell operating up to 4C [25]. As mentioned despite the importance of the ambient temperature only a few studies considered it. Smith et al. [26] developed a mathematical model coupling the1D electrochemical model to the lumped thermal model. They employed temperature dependent electrochemical properties in their model through application of the Arrhenius expression. Their model was validated for a 6 Ah, LCO/graphite lithium ion battery at 1C charge and discharge. They have also adapted the single cell model to model a battery pack containing 72 serially connected cells and the heat generation for a range of driving cycles and operating temperatures (e.g. −15 to 65°*C*). Wu et al. [27] developed a similar model using the same electrochemical parameters as in Ref. [26] and employed the model for investigation of the load

imbalance within the parallel cells of a battery pack. Farag et al. [28] succeeded to make a real-time prediction of a 26 Ah battery's core temperature and terminal voltage employing a combined electrochemical, heat generation and thermal model. However, the details of the electrochemical parameters have not been reported in their research. The model was validated over a broad range of C-rates and ambient temperatures ($-25°C$ - $45°C$), with $\pm$ 80 mV accuracy for terminal voltage and $\pm$ 2% error for the core temperature. As the thermal model is in 1D their model is potentially well suited for real time BMS applications. However, predicting the core temperature is not sufficient for designing a TMS, as the temperature gradient within the cell is arguably more crucial than the core temperature, especially when it comes to large format cells. The topic of absolute cell temperature vs. the impact temperature gradients is discussed further in Refs. [10,29]. But still there is lack of information on how these two are related under different operating conditions.

For EV applications, large format batteries with high energy and high power densities are more desirable as they extend EV driving range and also provide a more compact design for the pack [30]. However, large format batteries are more susceptible to a larger temperature gradient within the battery surface due to longer heat paths that may cause localised degradation [31]. The performance of large format batteries common to EV applications has not been extensively reported within the literature, with most studies focussed on simulating either lower capacity cells (typically: 10.5–14 Ah) or smaller form-factor cells [32]. Whereas choosing the right cell size for EV application is still a challenge as relative merits of large format cells are not well known [4,11]. Moreover, the models discussed within the literature are often only validated over a constant charge or discharge not using real world duty cycles. The impact of ambient temperature on the capacity fade, or power loss of a cell in real world scenarios has equally not been widely discussed. Even though such detailed information is vital for safe operation, extended lifetime of the cells, battery thermal management system and final cost of a battery pack and therefore cannot be ignored, noting that these are currently challenges to be overcome for commercialisation of EVs. Finally, derivation of the electrochemical parameters of the cell is often missing with researchers using data-sets from literature, where the provenance is not well defined and often resorting to using multiple sets of parameters from different sources to parameterise their models.

The contribution of this paper is therefore twofold. Firstly, it provides a validated modelling and simulation framework to study the

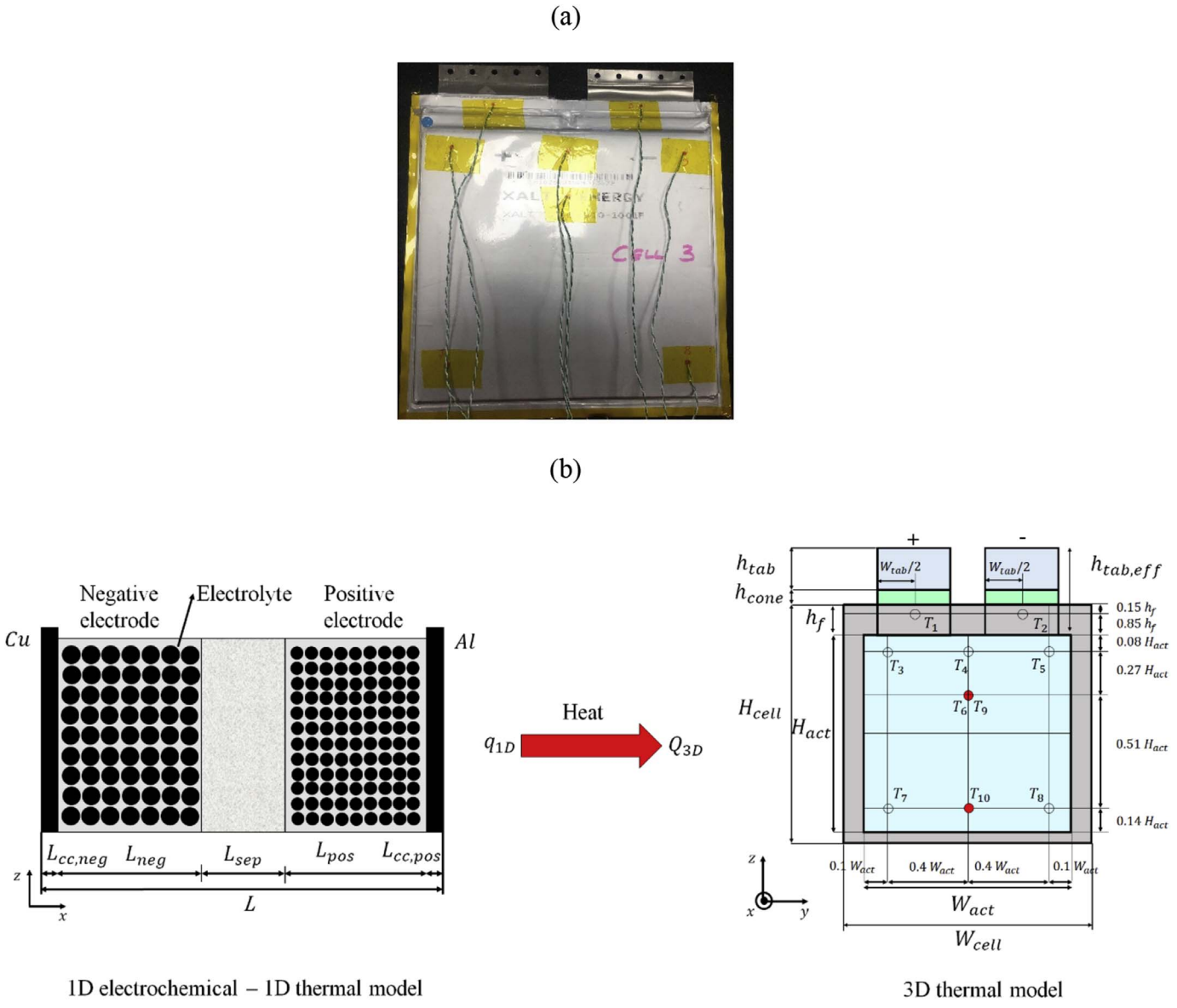

Fig. 1. (a) The schematic of the cell manufactured by XALT ENERGY, (b) Coupling of the 1D electrochemical-1D thermal model with the 3D thermal model.

electrical and thermal performance of large format pouch cells under real-world EV conditions, where variations in the ambient temperature on available cell energy capacity and power can be quantified. For the first time, a model is developed and validated employing real world duty cycles, including aggressive driving conditions, across a wide range of ambient temperatures (5–45°C) in addition to conventional methods of constant charge and discharge. Further, through a comprehensive experimental programme, a full parameter set for the model is defined and presented which is quite novel. This differentiates the developed model from the other models that currently exist in literature which employ parameters from different sources, which may not be relevant to the actual cell studied. Therefore, the model and underpinning parameterisation data are a valuable resource to other researchers seeking to design their own electrochemical-thermal models for both cell and system level analysis.

The study is structured as follows, Section 2 discusses the mathematical model including the 1D electrochemical-thermal model and the 3D thermal model. Section 3 defines the complete data set for the model, Section 4 and 5 present the experimental set up required for model characterisation and validation. Section 6 presents the reference model validated against the experimental data. Further work and conclusions are discussed in sections 7 and 8 respectively.

2. Model formulation

The electrochemical-thermal model within this study is based on the Pseudo Two-Dimensional (P2D) battery model which is a common approach for modelling li-ion batteries [33,34]. A battery cell consists of a different number of electrode pairs. The representative domain for the coupled 1D electrochemical-thermal model consists of one pair including a negative current collector, negative electrode, separator, positive electrode and a positive current collector. A P2D model solves for five variables namely; lithium concentration in the solid (C_s), and electrolyte phase (C_e), along with potential in the solid (ϕ_s), electrolyte phase (ϕ_e) and volumetric reaction current (j^{Li}), employing charge conservation, mass conservation, electrochemical kinetics and energy conservation equations [22,27]. Additional outputs from the model are terminal voltage (V_t), generated heat (Q), battery state of charge (SOC) and temperature (°C). In the is study, first the 1D electrochemical model is coupled with a 1D thermal model, hence the temperature dependency of the electrochemical parameters is considered when solving the electrochemical equations. The reason for coupling the electrochemical model with a 1D thermal model is to reduce the computational cost. Further the developed 1D electrochemical – 1D thermal model for one pair from step 1 is combined with a 3D thermal model of a cell sequentially in order to capture the temperature distribution in the cell scale. In essence, the 1D electrochemical-thermal model provides a heat source (generated heat from a constant charge/discharge cycle or a drive cycle) for the 3D thermal model in the cell level. The schematic of the cell and coupling between the 1D and the 3D model of the cell is depicted in Fig. 1. The total heat generation of the battery applied in the 3D model ($Q_{3D}(W)$, can be evaluated by tabulating the total volumetric heat generated form one electrode pair ($q_{1D}(W\ m^{-3})$ as follows:

$$Q_{3D} = q_{1D} \times N_{pairs} \times L \times A_{surf} \tag{1}$$

where N_{pairs} represents the number of electrode pairs in a cell, L is the thickness of one pair and A_{surf} ($W_{act} \times H_{act}$), is the surface area of the cell.

2.1. Cell specification

The li-ion batteries characterised in this study are commercial 53 Ah large format pouch cells manufactured by XALT ENERGY. The anode is made of graphite (LiC_6) and the cathode chemistry is $LiNi_xMn_yCo_{1-x-y}O_2$ (NMC). The lower and upper limit voltage during discharge and charge are 2.7V and 4.2V respectively. The maximum C-rate is 5C for continuous discharge and 2C for continuous charge, which is in accordance with the manufacturer's recommendation. The operating temperature range is between -20°C and 60°C for discharge and between 0°C and 45°C for charge. The dimensions of the cell are 225 mm × 225 mm × 11.8 mm.

2.2. 1-D electrochemical model

The derivation of the electrochemical model is discussed in detail within [35] for a 10 Ah LFP pouch cell and will therefore not be repeated here. For completeness, the governing equations and the boundary conditions that represent the P2D model are listed in Table 1.

2.3. 3-D thermal model

As the dynamic performance of a battery cell is related to its temperature, an accurate electrochemical-thermal model would assist in the optimal design of the battery and underpins the development of an efficient TMS. The 3D model geometry contains one cell with both tabs, as shown in Fig. 1. The bulk layer approximation of the complete cell is retained and the effective thermal properties of the bulk layer are

Table 1
Governing equations and boundary conditions for the P2D modelling framework.

Description	Governing equations	Boundary conditions	
Current of one electrode pair	$I_{pair} = \frac{\delta_{cell} \cdot C-rate}{N_{pairs}}$		(2)
Mass conservation: lithium in the solid phase	$\frac{\partial (C_s)}{dt} = \frac{D_s}{r^2}\frac{\partial}{\partial r}\left(r^2\frac{\partial C_s}{\partial r}\right)$	$\left.\frac{\partial C_s}{\partial r}\right\|_{r=0} = 0 - D_s\left.\frac{\partial C_s}{\partial r}\right\|_{r=r_p} = \frac{j^{Li}}{a_s F}$	(3)
Mass conservation: lithium in the electrolyte phase	$\frac{\partial(\varepsilon_e C_e)}{dt} = \nabla.\ (D_e^{eff}\nabla C_e) + \frac{1-t_+^0}{F} j^{Li}$	$\left.\frac{\partial C_e}{\partial x}\right\|_{x=L_{cc,neg}} = 0\left.\frac{\partial C_e}{\partial x}\right\|_{x=L-L_{cc,pos}} = 0$	(4)
Electronic charge balance: potential in the solid phase	$\nabla(\sigma^{eff}\nabla\phi_s) = j^{Li}$	$\phi_{cc}\|_{x=0} = 0 - \sigma_{cc}\nabla\phi_{cc}\|_{x=L} = -I_{pair}\nabla\phi_s\|_{x=L_{cc,neg}+L_{neg}} = 0$ $\nabla\phi_s\|_{x=L_{cc,neg}+L_{neg}+L_{sep}} = 0$	(5)
Electronic charge balance: potential in the electrolyte Phase	$\nabla(k^{eff}\nabla\phi_e) + \nabla(k_D^{eff}\nabla lnC_e) + j^{Li} = 0$	$\left.\frac{\partial\phi_e}{\partial x}\right\|_{x=L_{cc,neg}} = 0\left.\frac{\partial\phi_e}{\partial x}\right\|_{x=L-L_{cc,pos}} = 0$	(6)
Electrochemical Kinetics: reaction current density	$j^{Li} = a_s i_0\left\{exp\left[\frac{\alpha_a F}{RT}\eta\right] - exp\left[-\frac{\alpha_c F}{RT}\eta\right]\right\}$		(7)
Reaction surface area	$a_s = \frac{3\varepsilon_s}{r_P} = \frac{\left(1-\varepsilon_e-\varepsilon_f\right)}{r_p}$		(8)
Exchange current density	$i_0 = k_i(C_e)^{\alpha a}(C_{surf,max} - C_{surf,e})^{\alpha a}(C_{surf,e})^{\alpha c}$		(9)
Overpotential	$\eta_i = \phi_{s,i} - \phi_{e,i} - U_{ref,i}$		(10)

calculated based on this approximation through the use of literature equations and available experimental data. The input for the heat generation of the cell core comes from the electrochemical model. The heat balance for the cell is derived by application of the energy conservation principle as:

$$\rho C_p \frac{\partial T}{\partial t} = \frac{\partial}{\partial x}\left(k_x \frac{\partial T}{\partial x}\right) + \frac{\partial}{\partial y}\left(k_y \frac{\partial T}{\partial y}\right) + \frac{\partial}{\partial z}\left(k_z \frac{\partial T}{\partial z}\right) + q''' \tag{11}$$

where k_x, k_y, k_z are the effective thermal conductivities along the x (through the thickness), y (along the width) and z (along the height) direction. The terms ρ and C_p represent the equivalent density and heat capacity of the cell. q''' is the total volumetric heat generation within the cell which, as discussed within [36,37], is assumed uniform throughout the cell.

2.3.1. Heat source

The overall heat source of the cell (Q) is the result of the reversible heat (Q_{rev}), the irreversible heat (Q_{irr}) and the heat generation of the tabs (Q_{tab}), as displayed below:

$$Q = Q_{irr} + Q_{rev} + Q_{tab} = I.\,(U_{OCV} - V_t) - I.\,T.\,\frac{\partial U_{OCV}}{\partial T} + (R + R_c).\,I^2 \tag{12}$$

2.3.1.1. Reversible and irreversible heat source. The reversible heat of the electrodes is due to entropy change and can be either positive or negative [38–41]. A recent study reported that the entropy value is very much dependent on the cell chemistry, for example LiCoO2 has a much larger entropy variation compared to NMC or LiFePO4 (LFP) [42]. To find the entropic coefficients, the open circuit potential (OCP) measurement at different ambient temperatures is required [42–44]. However, the entropic terms used in this study are based on entropy measurements for a full cell not the individual electrodes. The irreversible heat (Q_{irr}), is attributed to the total heat generated in the electrodes, separators and current collectors as a result of electrochemical reaction and ohmic (electronic and ionic) potential drop. In general, Q_{irr} includes both reaction heat (Q_r) and ohmic heat (Q_{ohmic}). The ohmic heat itself consists of ionic ($Q_{ohmic,ionic}$) and electronic ($Q_{ohmic,\,elec}$). The irreversible heat can be evaluated as:

$$Q_{irr} = Q_r + Q_{ohmic,ionic} + Q_{ohmic,\,elec} = j^{Li}(\phi_s - \phi_e - U_{ref}) + \sigma^{eff}\nabla\phi_e\nabla\phi_e \;\text{ or }\; i_e^2/\sigma^{eff} + i_s^2/\sigma^{eff} \tag{13}$$

where i_e and represent the ionic and electronic current density respectively. The above equation is normally used for a detailed study on the heat generation of different sources and its distribution inside a cell [45]. However in a cell scale a more general term is often used [46]:

$$Q_{irr} = I.\,(U_{OCV} - V_t) \tag{14}$$

which has the same value as Eq (13), and accounts for all the heat generated in the cell as a result of electrochemical reaction or ohmic (joule) heating.

In the absence of active cooling, the convective boundary condition applied to the cell surface exposed to the ambient air is defined by:

$$q'' = h(T - T_{amb}) \tag{15}$$

where h ($W/(m^2.\,K)$) is the heat transfer coefficient, T is the surface temperature of the cell and T_{amb} represents the ambient temperature around the cell and q'' the heat flux at the exposed cell surface. A h value of 6 ($W/(m^2.\,K)$ provided the best fit to the experimental data. Similar approaches have been adopted in Refs. [11,47,48]. An insulation condition is specified on the back of the cell.

2.3.1.2. Heat generation of the tabs. The generated heat in the tabs is mainly due to ohmic resistance as well as a change of cross-section in the tab area in contact with the current collector [25]. The schematic of the cell geometry applied for the 3D model is presented in Fig. 1. The dimensions of the cell ($H_{cell} \times W_{cell}$) are adjusted to account for the active area ($H_{act} \times W_{act}$) of the cell contributing to the electrochemical reaction. Likewise, the height of the tab is adjusted so that it matches the cell height. The detailed dimensions of the cell are presented in Section 3. The heat generation of the tabs (Q_{tab}) is the result of ohmic and electrical contact resistances and is defined as below:

$$Q_{tab} = (R + R_c).\,I^2 \tag{16}$$

where R (Ω) is the resistance of the current collector and R_c (Ω) denotes the electrical contact resistance between the current collecting tab and the lead wire which connects the cell to the battery cycler [15]. It should be noted that except for the edge of the current collecting tab contacting with the lead wire, R_c is zero and the heat generation is only due to the ohmic resistance [49]. R is dependent on the tab dimensions and tab material and is defined by Refs. [15,17]:

$$R = \rho\frac{h_{tab,eff}}{A_{tab,eff}} \tag{17}$$

where ρ ($\Omega.\,m$) is the resistivity, $h_{tab,eff}$ (m) and $A_{tab,eff}$ (m^2) define the height and effective cross section area of the tab respectively. It is noteworthy that, $A_{tab,eff}$ accounts for the area of the tab in all the layers inside the cell and therefore is calculated as:

$$A_{tab,eff} = N_{pairs} \times (h_{tab,eff} \times w_{tab}) \tag{18}$$

where N_{pairs} is the number of pairs inside the cell. These resistance parameters can be either measured or obtained from the battery manufacturer [17]. It is difficult to measure R_c through experiments and hence, it is often neglected [25]. However R_c has a much larger value than R, resulting in a significant contribution to the heat generation of the tab. Similar to the study reported by Yi et at. [49], in this study R_c is adjusted to get the best modelling fit to the experimental data, by checking the brass block (cell connector to the battery cycler) temperature. Table 4 summarises the parameters applied in this study to evaluate the total heat generation from the tabs.

2.3.2. Thermal parameters

The density of the cell is calculated by dividing the total mass of the cell by its volume. The thermal conductivity of the cell is orthotropic due to its layered structure and containing multiple materials with different thickness and thermal properties. The effective thermal conductivity through the thickness of the cell (x direction), as well as the y and z direction is given follows [50–53].

$$k\perp = k_x = \frac{\sum L_i}{\sum \frac{L_i}{k_i}} \tag{19}$$

$$k_= = k_y = k_z = \frac{\sum kL_i}{\sum L_i} \tag{20}$$

where k_i and L_i represents the thermal conductivity as well as the thickness of the internal layers of the cell. Comparing the calculated k_x with the experimental values reported within the literature (0.15–0.2 $W/(m.\,K)$) [54], (0.25 $W/(m.\,K)$) [55]. However, Eq. (16) is not used to determine the cross-plane thermal conductivity, given that it neglects the presence of contact resistances between the cell layers, that would result in an over prediction in the thermal conductivity value [56]. As such, literature values for the cross-plane thermal conductivity value are used. The thermal property values used for the lumped 3D thermal model are summarised in Table 5.

3. Definition of dataset for the 1-D electrochemical model and the 3-D thermal model

The 1-D electrochemical model parameters can be categorised in to two groups. The first group includes the physical properties of the

Table 2
The electrochemical parameters of the 53 Ah pouch cell with NMC chemistry.

Parameters	Negative electrode	Separator	Positive electrode
Constant parameters			
Bruggeman porosity exponent, $brugg_n$	1.5 [22,27]		
Universal gas constant, R_{uni}	8.314		
Faraday's constant	96485		
Design specification			
Thickness, L (μm)	74.83[a]	17[a]	41.16[a]
Particle size, r_p (μm)	26.2[a]		10.7[a]
Volume fraction of the active material, ε_s	0.58 [22]		0.43 [22]
Volume fraction of the electrolyte, ε_e	0.32 [22]	0.54 [22]	0.32 [22]
Maximum lithium concentration in the solid phase, $C_{s,\,max}$ $(mol\ m^{-3})$	29802[b]		87593[b]
Electrolyte lithium concentration, $C_{e,\,max}$ $(mol\ m^{-3})$		1200 [22,27]	
Stoichiometry at SOC = 1, x_1, y_1	0.75[b]		0.38[b]
Stoichiometry at SOC = 0, x_0, y_0	0.05[b]		0.93[b]
R_{SEI} $(\Omega.cm^2)$	20		20
Lithium ion transference number, t_+^0	0.363	0.363	0.363
Electrolyte activity coefficient, $f_{\pm}$	1 [27]	1 [27]	1 [27]
Charge transfer coefficient, α	0.5 [27]		0.5 [27]
Dynamic parameters			
Lithium diffusion coefficient in the negative electrode, $D_{s,\,neg}$ $(m^2\ s^{-1})$	$D_{s,\,neg} = 3\times10^{-13}\exp\left(\frac{-E_{act}^{Ds-}}{R}\left(\frac{1}{T}-\frac{1}{298.15}\right)\right)^2$	(22)	
Lithium diffusion coefficient in the positive electrode, $D_{s,\,neg}$ $(m^2\ s^{-1})$	$D_{s,pos} = 7\times10^{-14}\exp\left(\frac{-E_{act}^{Ds+}}{R}\left(\frac{1}{T}-\frac{1}{298.15}\right)\right)^2$	(23)	
Lithium diffusion coefficient in the electrolyte, $D_{s,\,neg}$ $(m^2\ s^{-1})$	$D_e = 3.8037e-10\times\exp(-0.78281\ C)\exp\left(\frac{-E_{act}^{De}}{R}\left(\frac{1}{T}-\frac{1}{298.15}\right)\right)$, [61]	(24)	
Reaction rate in the negative electrode, k_{neg} $(m\ s^{-1})$	$k_{neg,discharge} = k_{0,neg}^{dis}exp\left(\frac{-E_{act}^{k}}{R}\left(\frac{1}{T}-\frac{1}{298.15}\right)\right)^2$	(25)	
	$k_{neg,charge} = k_{0,neg}^{ch}\exp(-5x)exp\left(\frac{-E_{act}^{k}}{R}\left(\frac{1}{T}-\frac{1}{298.15}\right)\right)^2$		
Reaction rate in the positive electrode, k_{pos} $(m\ s^{-1})$	$k_{pos,discharge} = k_{0,pos}^{dis}\exp(-5y)exp\left(\frac{-E_{act}^{k}}{R}\left(\frac{1}{T}-\frac{1}{298.15}\right)\right)^2$	(26)	
	$k_{pos,charge} = k_{0,pos}^{ch}exp\left(\frac{-E_{act}^{k}}{R}\left(\frac{1}{T}-\frac{1}{298.15}\right)\right)^2$		
Electrolyte ionic conductivity, κ $(S\ cm^{-1})$	$\kappa = 15.8\times c_e.\ \exp(-13472Ce^{1.4})exp\left(\frac{-E_{act}^{\kappa}}{R}\left(\frac{1}{T}-\frac{1}{298.15}\right)\right)^2$ [27]	(27)	
Open circuit potential of the negative electrode	$U_{ref,neg} = 0.6379 + 0.5416\exp(-305.5309x) + 0.044\tanh\left(-\frac{x-0.1958}{0.1088}\right)$ [62] $- 0.1978\tanh\left(\frac{x-0.0117}{.0529}\right) - 0.0175\tanh\left(\frac{x-0.5692}{0.0875}\right)$,	(28)	
Open circuit potential of the positive electrode	$U_{ref,pos} = -10.72y^4 + 23.88y^3 - 16.77y^2 + 2.595y + 4.563$, [63]	(29)	
Local state of charge of the negative electrode, x	$x = SOC_{neg} = \frac{C_{s,surf,neg}}{Cs,\,max,\,neg}$	(30)	
Local state of charge of the positive electrode, y	$y = SOC_{pos} = \frac{C_{s,\,surf,pos}}{Cs,\,max,\,pos}$	(31)	

[a] Experiment.
[b] Estimation.

battery which are fixed in the model and the second group is the dynamic parameters which are known to be a function of temperature and SOC of the battery. This latter subset of parameters are, the reaction rate (k_i), the diffusion coefficient of Li in the solid active materials ($D_{s,i}$), the diffusion coefficient of Li in the electrolyte (D_e), the electrolyte ionic conductivity (κ), open circuit potential and entropy change [57]. A common approach for temperature dependent parameters is to describe them by the Arrhenius equation [21,26,45,57–60].

$$\psi = \psi_{ref}\,exp\left[\frac{E_{act,\psi}}{R_{uni}}\left(\frac{1}{T_{ref}}-\frac{1}{T}\right)\right] \tag{21}$$

where T is the temperature and R_{uni} is the universal gas constant. ψ represents a general parameter, which can be diffusion coefficient, reaction rate, ionic conductivity, and $E_{act,\psi}$ represents the corresponding activation energy. The magnitude of $E_{act,\psi}$ shows the sensitivity of the parameter to the temperature [58]. Among these model variables, the parameters with strongest temperature dependency are the solid phase diffusion coefficient and the reaction rate that affects the charge transfer resistance. The electrochemical model contains a large number of parameters, which some of those are chemistry dependent whereas the others are specific to the cell. Table 2 presents the full set of

Table 3
Dimensions of the cell corresponds to Fig. 1.

Domain	Height (mm)	Width (mm)	Thickness (mm)
Pouch cell	$H_{cell} = 225$	$W_{cell} = 225$	$t_{cell} = 11.8$
Active area	$H_{act} = 184$	$W_{act} = 208$	$t_{act} = 11.8$
Tab	$h_{cone} = 10h_f = 35$	$W_{tab,pos} = 80$	$t_{tab,pos} = 0.725$
	$h_{tab} = 32$	$W_{tab,neg} = 80$	$t_{tab,neg} = 0.464$

electrochemical parameters used in this study. The next section elaborates how the parameters were quantified.

The following section presents all the physical and thermal properties of the cell applied in this study. The detailed dimensions of the cell are presented in Table 3.

The parameters applied in this study to evaluate the total heat of the tabs are presented in Table 4.

The thermal property values used for the lumped 3D thermal model are summarised in Table 5.

4. Experimental derivation of constant model parameters

As discussed within [35,62], out of the large number of electrochemical parameters electrode thickness (L_i), particle sizes (r_p), porosity (ε_i), diffusion coefficient (D_i), lithium concentration in the active materials ($C_{s,max}$) and reaction rate (k_i) in both electrodes are found to be the most crucial ones for modelling. It should be noted that i indicates the domain. Only a subset of the above parameters are directly measurable, such as (L_i) and (r_p). Other parameters are difficult to measure directly, but they may be calculated. For example by measuring the (r_p), (D_i) can be estimated. Similarly (ε_i), is difficult to measure or calculate. However, after estimating that from literature data, ($C_{s,max}$) can be calculated. Finally, the reaction rates (k_i) are applied as the fitting parameters as they can be neither measured or calculated. Following the discussion above a set of experiments were conducted to characterise the cell and find the electrochemical parameters. The initial experiments include battery tear down and scanning electron microscopy (SEM) to find the number of layers, thickness and dimensions of each layer and the particle sizes.

4.1. Number of layers and thickness

A new cell was discharged only once to 2.7 V at 25 °C from its initial condition of 50% SOC. The cell was then opened in an argon filled glovebox (O2 and H2O below 0.1 ppm), and remained there for 24 h for the electrolyte to evaporate. After this stage, all the layers were detached and the most proper sample including cathode, separator and anode layers was chosen for measuring the thickness. The measurements were repeated for 3 times and the average value of the thickness was obtained for further analysis. The maximum measurement error was 1 μm. The complete procedure is presented in Fig. 2(a,b).

It was observed that the cell was manufactured by sequentially repeating the layers in the following format: anode (dual face) + separator + cathode (dual face) + separator + cathode (dual face) + separator + … + anode dual face). The cell contained 60 negative electrodes, 30 negative current collectors, 58 positive electrodes, 58 separators and 29 positive current collectors. The dimensions of the layers is given in Table 6 and Table 7.

4.2. Particle sizes

A small sample (1 × 1 cm) of the negative and positive electrodes were cut and washed with DMC (di-methyl carbonate) for further use. SEM images were obtained using a Carl Zeiss Sigma Field Emission Scanning Electron Microscope (FE-SEM) at 5 kV accelerating voltage in combination with in-lens detection at working distances of approximately 2 mm. The SEM images of the anode and cathode are presented in Fig. 3(a,b). The SEM images show a non-uniform particle sizes within both electrodes, therefore several measurements within the samples were made and the average sizes were employed for the modelling as displayed in Table 8.

Table 4
Resistance values applied for the positive and negative tab of the 53 Ah NMC pouch cell.

Parameter	Negative tab	Positive tab
ρ (Ω. m) [17]	1.68×10^{-8}	2.54×10^{-8}
$h_{tab,eff}$ (m)	0.077	0.077
$A_{tab,eff}$ (m^2)	3.71×10^{-5}	5.80×10^{-5}
R (Ω)	3.48×10^{-5}	3.37×10^{-5}
R_c (Ω)	3.40×10^{-5}	6.37×10^{-5}

4.3. Other parameters

The particle sizes were defined based on the average values obtained from SEM images. The performance of the battery is highly dependent on the particle size, likewise the electrochemical model is very sensitive to this parameter. Therefore, in terms of validity of the model it is important to use the measured values in the model. On the other hand, there is a correlation between the particle size and the diffusion coefficient. The lower limit of the diffusion coefficient in the solid phase can be defined by the following equation.

$$\tau = \frac{t_{dis}}{t_{dif}} \tag{32}$$

where τ is the dimensionless time and compares the relative rates of the discharge and diffusion processes, t_{dis} is the discharge time of the cell until it reaches the cut off voltage. The diffusion time is the required time for intercalation of the lithium and is a function of particle size as well as diffusion coefficient, as described by equation (30).

$$t_{dif} = \frac{r_p^2}{D_s} \tag{33}$$

For the battery operation not to be limited by the diffusion coefficient in the solid phase, the dimensionless time has to be higher than 0.2 ($\tau > 0.2$) [64]. This reveals that for this 53 Ah cell operating up to 5C, the lower limit for the diffusion coefficient in the positive and the negative electrode is equal to 4.3×10^{-14} and 2.1×10^{-13} respectively.

Capacity of the positive and negative electrodes (δ_{pos}, δ_{neg}) are defined below, in accordance with [65].

$$\delta_{pos} = \varepsilon_{s,pos}.\ L_{pos}.\ A_{pos}.\ C_{smax,pos}.\ (x_1 - x_0).\ F, \tag{34}$$

$$\delta_{neg} = \varepsilon_{s,neg}.\ L_{neg}.\ A_{neg}.\ C_{smax,neg}.\ (y_0 - y_1).\ F \tag{35}$$

A_i is the active area of the electrodes and F is the Faraday's constant. x_0, y_0 are the initial stoichiometry values for the negative and positive electrodes respectively at (SOC = 0), and x_1, y_1 represent the stoichiometry values at (SOC = 1). Assuming that the positive and negative electrodes have identical capacities equal to that of the cell, $C_{smax,pos}$ and $C_{smax,neg}$ can be found. The reaction rates, k_{pos} and k_{neg} are the adjusting parameters to fit the charge and discharge curve obtained from the experimental measurements.

5. Experimental derivation of dynamic model parameters

The experiments undertaken include the open circuit voltage (OCV) measurements and capacity test including charge and discharge under different C-rates at temperatures of 5 °C–45 °C. This was conducted to find the adjusting parameters (k_i), and the activation energy for temperature dependent parameters ($E_{act,\psi}$) in the Arrhenius function and to validate the 1D electrochemical model. The model parameters as provided in Table 9.

Finally, the surface temperature of the battery was measured by employing 10 temperature sensors (as displayed in Figure 1, 8 on the front (T_1-T_8) and two at the back surface of the cells (T_9, T_{10})), and a thermal camera to validate the thermal model. To conduct the experiments, 3 cells were placed in a thermal chamber (Weiss Gallenkamp Votsch VC3 4060). The air was circulated within the thermal chamber by an electric fan to keep the temperature constant. The cells were connected to a commercial cycler namely a Bitrode MCV 16-100-5 to perform the test protocols. To make a stable connection, the cells were

Table 5
Thermal parameters used for the 53 Ah NMC pouch cell.

Material/ component	Density ρ (kg/m^3)	Heat capacity C_p $(J/(kg.\ K))$	Thermal conductivity k $(W/(m.\ K))$
Pouch cell	2551.7	1100	$k_x = 0.28$ [36] $k_y = 28 k_z = 28$

placed horizontally inside the chamber in contact with Acrylic sheets of 12 mm thickness, with the top surface exposed to the air flow, so that only the underside of the cell is in contact with the sheet. The position of the cells within the thermal chamber is presented in Fig. 4.

5.1. OCV measurement

The open circuit voltage was collected from the cells potential measurements during a 1C discharge from 100% to 0% SOC. 0% SOC corresponds to when the cut off voltage of 2.7 was reached. The cells were discharged for 144s (0.04% SOC) at each single step accompanied by 4 h rest period. The terminal voltage of the cells was measured at the end of the rest periods. The OCV of the cells were measured during the discharge process at 5, 25 and 45^oC to find the entropic coefficients contributing to the reversible heat. Entropy measurements for either individual electrodes or full cell of different chemistries determines that the entropy magnitude and its deviation by SOC for one cell can significantly differ from one another [42]. Looking at OCV deviation of the cells by temperature (displayed in section 6.1.1, Fig. 6(b)) over the discharge events, the entropy effect can be achieved. The trend is similar to the one presented by Viswanathan et. Al [42]. It is seen that for (SOC $>$ 0.7), the entropy variation is positive indicating that the reaction is endothermic, and for (SOC $<$ 0.7), entropy variation over temperature is negative, proving an exothermic reaction. The magnitude of entropy significantly increases for (SOC $>$ 0.9). This confirms that the entropic heat is more noticeable at the end of discharge. The averaged entropy value over a full discharge event is equal to -0.64 (mV/K), which is negligible compared to the irreversible heat.

5.2. Charge and discharge

Each discharge rate measurement requires initialisation steps to precondition the cell before the measurement. At the first step the cells were discharged under a constant 1C discharge rate until a cut off voltage of 2.7V was reached. Then it was followed by a 4 h rest period to allow the cell to equilibrate [3,66]. Afterwards the cells were charged under a constant current-constant voltage (CC-CV) method.

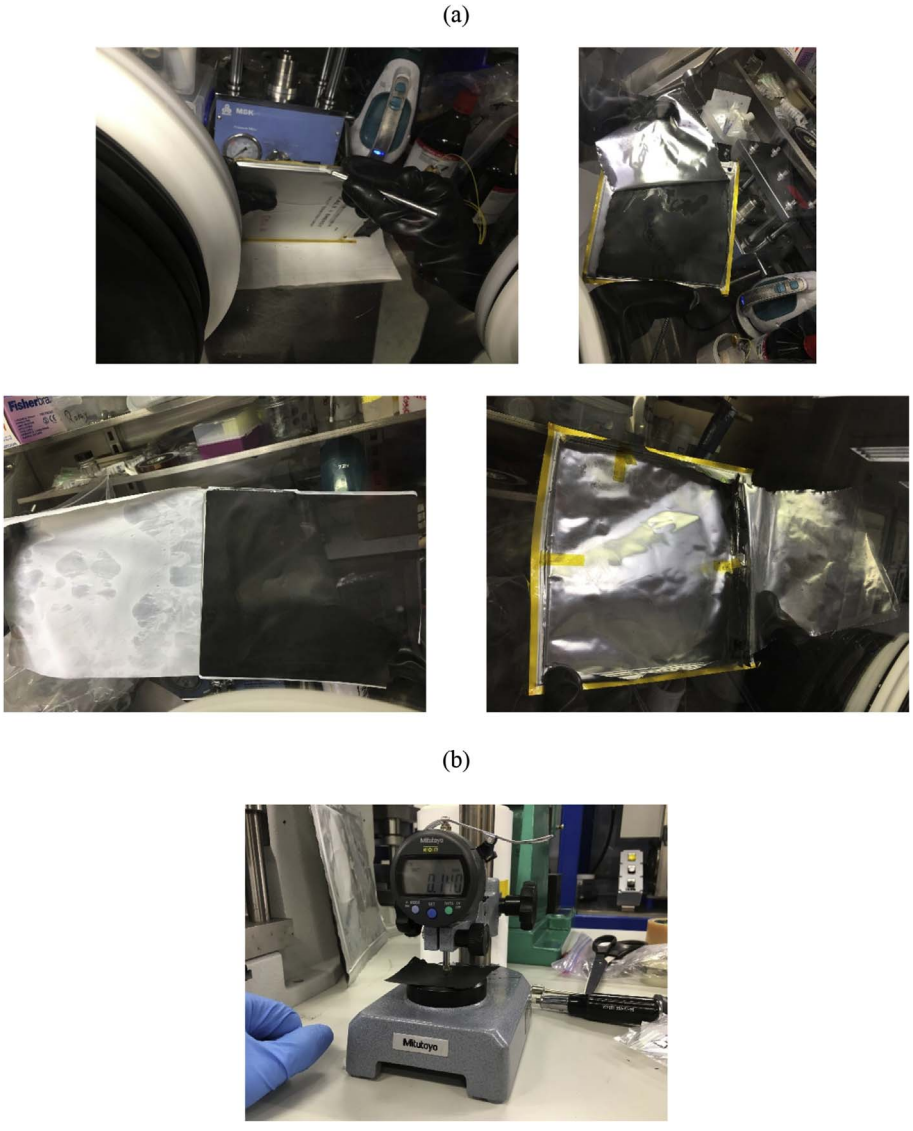

Fig. 2. (a) Tear down of the 53 Ah NMC pouch cell, (b) Instruments for measuring the thickness of the layers.

Table 6
Thickness of the individual layers inside the 53 Ah NMC pouch cell.

Parameter	Measurement 1 (mm)	Measurement 2 (mm)	Measurement 3 (mm)	Average (mm)
$2 \times L_{cc,pos}$	0.027	0.025	0.023	0.025
$2 \times L_{cc,neg}$	0.015	0.018	0.015	0.016
$2 \times L_{cc,pos} + 2 \times L_{pos} + 2 \times L_{sep}$	0.14	0.143	0.143	0.142
L_{sep}	0.018	0.017	0.017	0.0173
$2 \times L_{cc,neg} + 2 \times L_{neg}$	0.169	0.163	0.165	0.1656

Table 7
Average values for the thickness and area of all subdomains inside the 53 Ah pouch cell.

Domain	Thickness (μm)	Area ($mm \times mm$)
Negative current collector (cc, neg)	8	208 × 188
Negative active material (neg)	74.83	208 × 188
Separator (sep)	17	204 × 184
Positive active material (pos)	41.16	204 × 184
Positive current collector (cc, pos)	12.5	204 × 184

Table 8
The particle size of the negative and positive electrode obtained through SEM.

Measurement	Anode $r_{p,neg}$ (μm)	Cathode $r_{p,pos}$ (μm)
1	19.5	8.9
2	25.1	10.02
3	28.1	11.3
4	32.2	12.5
Average	26.2	10.7

Table 9
Reaction rates and the activation energy of the dynamic parameters defined through experiments.

Parameter	Value
Discharge reaction rate, $k_{0,neg}^{dis}$, $k_{0,pos}^{dis}$	5×10^{-10}, 2.5×10^{-10}
Charge reaction rate, $k_{0,neg}^{ch}$, $k_{0,pos}^{ch}$	1.2×10^{-9}, 6×10^{-10}
Activation energy – solid phase diffusion coefficient, $E_{act}^{D_s-}$, $E_{act}^{D_s+}$ ($J\ mol^{-1}$)	35000
Activation energy – electrolyte diffusion coefficient, $E_{act}^{D_e}$ ($J\ mol^{-1}$)	10000
Activation energy – reaction rates, E_{act}^{k} ($J\ mol^{-1}$)	20000
Activation energy – electrolyte ionic conductivity, E_{act}^{κ} ($J\ mol^{-1}$)	20000

The CC section is followed by a 1C charge until the voltage reaches to 3.6 V and for the CV section, the voltage is held at 3.6 V until the current drops to C/20 [3]. Again a rest period of 4 h was applied for the cells, afterwards they were discharged until a cut of voltage of 2.7V was reached. The cells were discharged under constant discharge rates (0.5C, 1C, 2C, 3C and 5C), noting that 5C is the maximum discharge rate recommended by the manufacture. In total, 30 separate discharge test conditions were evaluated. For the charge procedure, likewise the discharge protocol, the cells need an initialisation step before the measurement started. That included a constant discharge until the cut off voltage of 2.7 V was reached, followed by a 4 h rest period. Afterwards the three fully discharged cells were charged at 5°C–45°C, following a CC-CV method at different C-rates, (0.5C, 1C and 2C). The 2C charge rate is the maximum limit recommended by the manufacturer. In total, 15 separate charge test conditions were evaluated. The terminal voltage of the cells were recorded at every second during both the charge and discharge events. The summary of the test protocols is displayed in Table 10.

The voltage response of the cells for the above discharge and charge protocols indicates that the cells behave very similarly during the whole process for the various range of ambient temperatures (5°C–45 °C). Therefore, only the results for cell 1 are presented here. The voltage of the cell during charge and discharge over different C-rates as well as ambient temperature is illustrated in Fig. 5(a,b). It is observed that as the temperature increases both the voltage and capacity of the cell increase. As discussed within section 1, this is due to the dependency of the electrochemical resistances to the temperature. It is known that the cells exhibit a very high resistance at low temperature which can be attributed to the slow kinetics of the cell reaction [67], whereas the resistance significantly decreases as the temperature rises. The

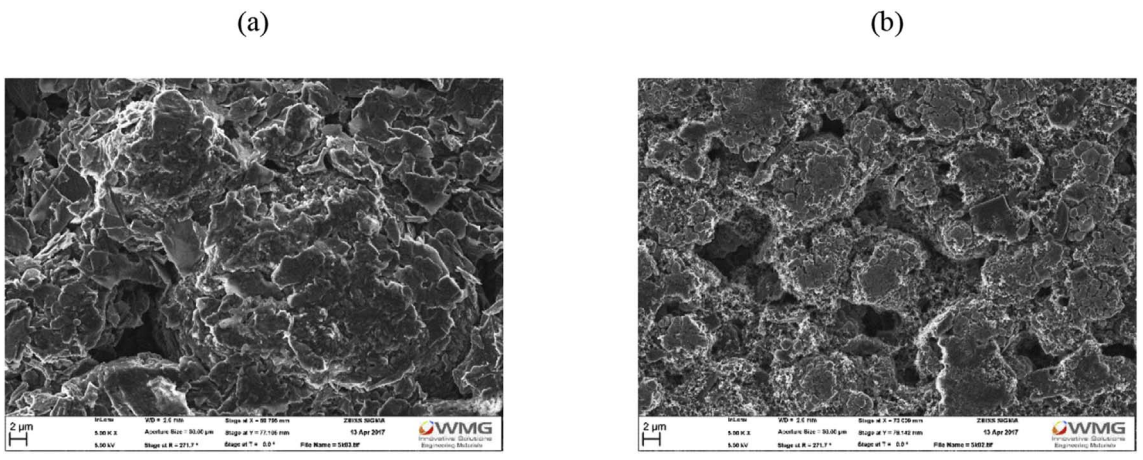

Fig. 3. SEM images of, (a) the negative active material (graphite) and, (b) The positive active material (NMC).

Fig. 4. (a) The position of the cells in the thermal chamber at 5°C–45°C, (b) Cells connections and insulation.

Table 10
Charge and discharge test protocols of the 53 Ah cell at different ambient temperatures.

Temperature	C-rate					
	0.5C	1C	2C	3C	4C	5C
5°C	D & C	D & C	D & C	D	D	D
15°C	D & C	D & C	D & C	D	D	D
25°C	D & C	D & C	D & C	D	D	D
35°C	D & C	D & C	D & C	D	D	D
45°C	D & C	D & C	D & C	D	D	D

temperature effect is more pronounced at high C-rates, where the cell over potential is higher.

6. Results and discussions

By applying the thermal and electrochemical parameters, a general parametric battery model was constructed. However, the underpinning model and experimental methods can be applied for batteries of different sizes or chemistries by reparametrizing the model. The following sections present the validation of the electrochemical and thermal model for the 53 Ah NMC cell. Moreover, variation of capacity and power over the ambient temperature is futher discussed.

6.1. Verification of the model

6.1.1. OCV tests/charge and discharge

The OCV of the cell is defined as the difference between the potential of the positive and the negative electrode. Ideally, the OCV is measured for each electrode separately. However, in this study the theoretical equations, presented in Table 2, were employed to represent the potential of each electrode locally. Then, the obtained OCV from the mathematical model was compared with the cell level measured OCV at 25 °C, as presented in Fig. 6(a). Variation of the OCV over the ambient temperature from experimental measurements is shown in Fig. 6(b). The terminal voltage of the battery under different constant charge and discharge rates at 25°C is presented in Fig. 6(b,c). The simulation data refers to the predicted voltage from the mathematical model and the experimental data were collected during cell operation. The results show the validity of the model for the whole operating range of the cell.

The total error can be obtained as follows:

$$error\ \% = \frac{V_{sim} - V_{exp}}{V_{exp}} \times 100 \quad (36)$$

V_{sim} is the terminal voltage obtained from the model and V_{exp} is the measured voltage. The results show a satisfactory agreement between the simulation and experimental data, with 5.7%, 6.4% and 1.2% peak error for OCV, discharge and charge events at 25°C. The accuracy of the model is comparable to other published studies as in general they show a higher inaccuracy at low SOC (below 0.2) or high C-rates [8,68–70].

6.1.2. Temperature

The results obtained from the thermal model were compared with those obtained from the experiments. A fully charged cell was discharged under 3C and 5C at 25°C. A FLIR T440 thermal camera recorded the surface temperature during the process. Fig. 7(a,b) compares the numerical results with the obtained experimental data. The model accurately predicts the temperature profile with a 6% error in peak temperature at the end of discharge for both 3C and 5C. The error can be attributed to either the assumption of uniform heat generation within the cell body or the accuracy of the thermal boundary conditions. The hot spots are generally expected to be close to the positive tab [13,47,71] whereas both the experimental and simulation results show that the hot spot is close to the cell centre in this study. The same phenomenon has been already reported by Grandjean et at. [3]. This is due to the large brass blocks, connecting the tabs to the cycler, which act as a heat sink, drawing the heat from the cell via conduction and dissipate it to the environment via convection [3]. To ensure that this is the case, a new set of simulations were conducted eliminating the brass block as presented in the third row of Fig. 7(a,b), (a_9-a_{12}, b_9-b_{12}). It is observed that at 3C until t = 800s the hot spot is close to the positive tab and it eventually moves towards the cell centre by the end of discharge. This is a similar observation to the results of Veth et al., where the migration of the hotspot occurs due to the effect of convective cooling on the edges of the cell [72]. Whereas during the 5C discharge the positive tab is always the hot spot. That is because the heat generation of the tab increases at a rate equal to the square of the current, its contribution to the total heat generation is therefore more pronounced.

6.2. Validation of the model - drive-cycle simulation/experimental work

Different charge and discharge protocols at different ambient

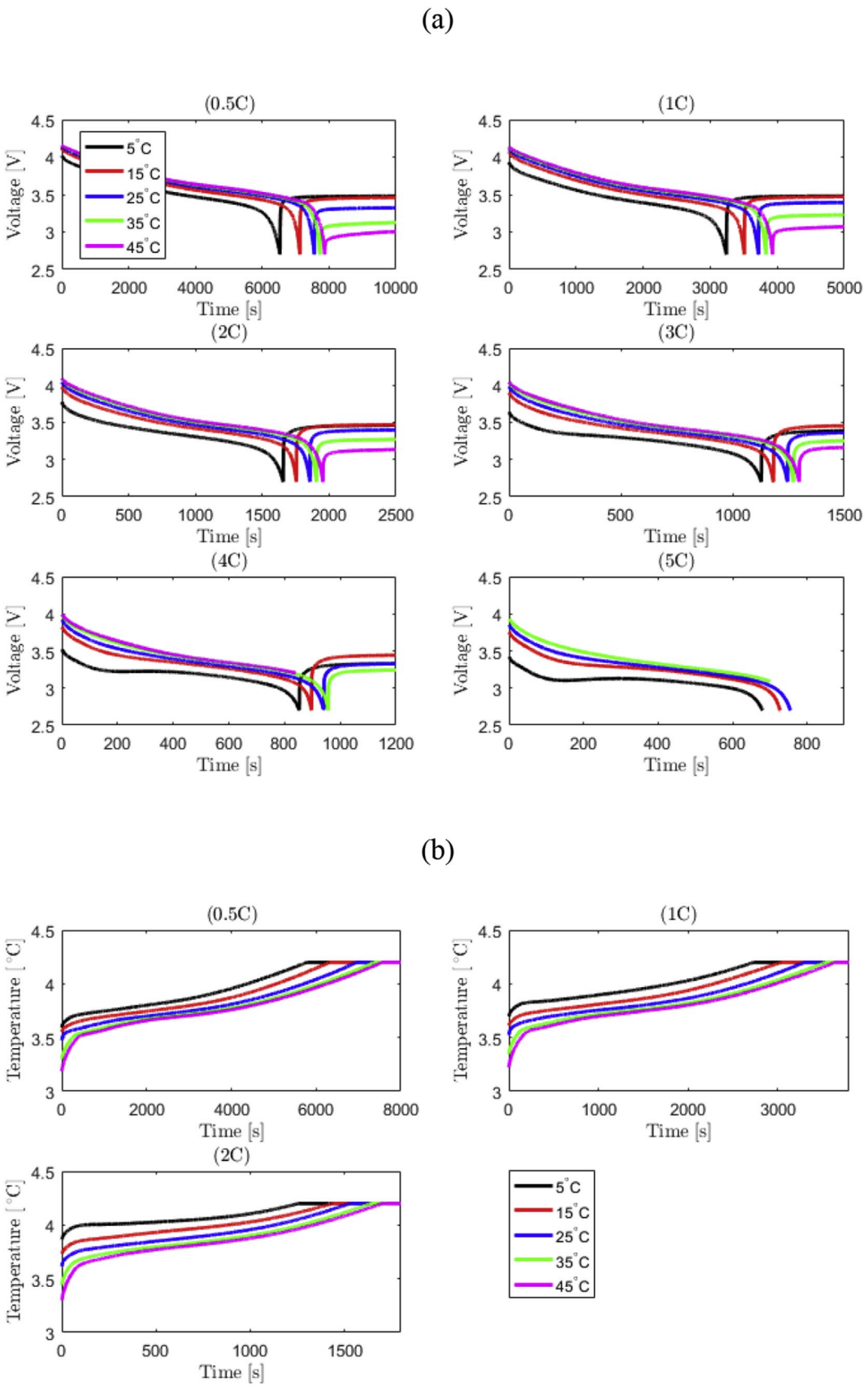

Fig. 5. (a) The voltage of the Xalt 53 Ah cell during discharge under (0.5–5C), and (b) Charge under (0.5–2C), at (5 °C −45 °C) ambient temperature.

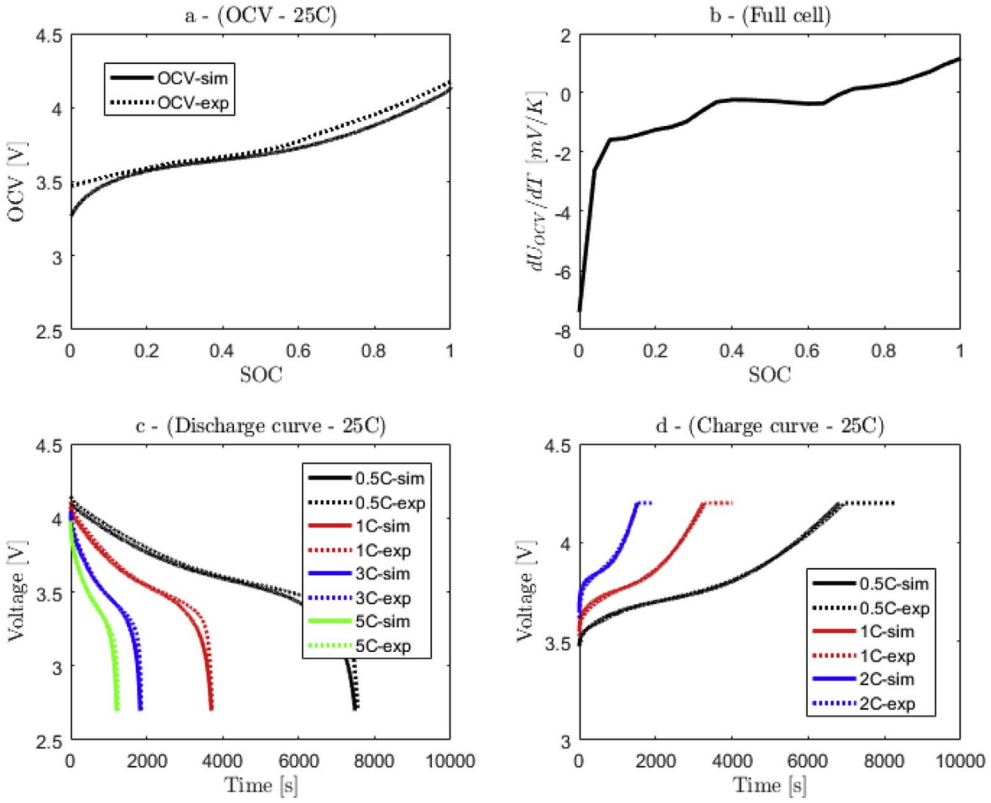

Fig. 6. (a) Comparison between the mathematical and the experimental OCV of the cell, (b) OCV variation over ambient temperature, model validation under (c) Discharge and, (d) Charge, at 25 °C ambient temperature.

temperatures help to understand the existing correlation between the battery resistance, load current as well as ambient temperature. However, to obtain a realistic estimation of the battery performance under various conditions, two drive cycles were applied, namely WLTP Class 3 and a high performance EV drive cycle. The methodology for construction of the EV race duty cycle is beyond the scope of this paper, however, details behind its derivation is discussed further in Ref. [37]. The tests started at initial SOC = 100% for both drive cycles and a final SOC of 0.2 and 0.05 was reached at the end of the race and WLTP Class 3 cycles respectively. The current profile, terminal voltage, total heat generation, SOC and maximum surface temperature (T_6 as displayed in Fig. 1) of the cells corresponding to the race and WLTP cycle at different ambient temperatures, (5 °C, 25 °C and 45 °C) is presented in Fig. 8(a,b). The results for the race cycle reveal that there is a significant voltage drop at 5 °C compared to 25°C and 45 °C operating temperature, especially at the beginning of the drive cycle until t = 800s, after that the rate of voltage reduction is monotonic. This can be attributed to the self-heating effect which causes a temperature rise in the cell and therefore reduces the internal resistance [6]. The heat generation follows the same trend as the terminal voltage as it is proportional to the voltage drop. The time averaged heat generation value is equal to 49.5 W at 5 °C while it drops to 30.3 W and 28.5 W at 25 and 45 °C ambient temperatures respectively, corresponds to 38.8% and 42.4% heat reduction. It is clear that low operating temperatures significantly deteriorates battery performance. It is noteworthy that even though higher operating temperatures are desirable in terms of power and capacity improvement, its impact for long term operation is not beneficial as it is known to accelerate battery aging [6,73]. The maximum surface temperature of the cells at the end of the race cycle where the SOC reaches to 0.2 is equal to 33.7°C, 44,6°C and 62.6 °C at 5°C, 25°C and 45 °C ambient temperatures respectively. The maximum temperature elevation is equal to 28.7 °C for 5 °C environmental conditions. This reduces to 19.6°C and 17.6°C under 25°C and 45 °C operational temperatures. As seen, the response of the battery to the load current is very different at low temperatures while the difference is not noticeable for temperatures above 25 °C. This further reinforces the importance of controlling the operating temperature of the battery, to avoid both high internal resistance as well as accelerated degradation rate.

Comparing the numerical and experimental terminal voltage of the cell corresponding to the race cycle, it is seen that the model can predict the cell behaviour very accurately during the whole cycle. At 25°C ambient temperature, the peak and average error is equal to 2% and 0.5% respectively. The model captures the cell voltage at 45°C accurately, with 1.7% peak error along with 0.5% average error. It is seen that at 5°C, there is a deviation between the voltages at the beginning of the cycle until t = 500s. In addition, the numerical voltage during the charge process is slightly higher from t = 1000s until the end of the duty cycle. This can be partly attributed to the OCV variation at 5°C compared to 25°C. Moreover as highlighted within section 1, the electrochemical parameters are highly temperature dependent, and the resistance of the cell behaves very differently at lower temperatures [67]. This phenomenon might not be fully captured through inclusion of the Arrhenius function to the equations. The peak error is equal to 16.1% at t = 363s, and the average error is 2.3% which is acceptable as the model covers a wide range of currents and temperatures.

For WLTP Class 3 which is more representative of urban and commuter operation than the high performance EV cycle, the batteries start operation at 100% SOC. The battery response to WLTP drive cycle is shown in Fig. 8(b). The measurements confirm that even with a gentle drive cycle the battery performance is very poor at low ambient temperatures. The low voltage of the cell at 5 °C leads to a higher heat generation, 13.8 W which is almost twice of that at 25 °C, equal to 6.3W. By rising the ambient temperature, the heat generation reduces further however the variation is not significant, equal to 5.1 W at 45 °C which is a 19% deduction. The maximum surface temperature of the batteries (T_6, displayed in Fig. 1), at the end of WLTP cycle, at 5% SOC is equal to 21.2°C, 34.5°C and 52.4 °C at 5°C, 25°C and 45 °C respectively. Moreover, the corresponding temperature rise of the cell surface

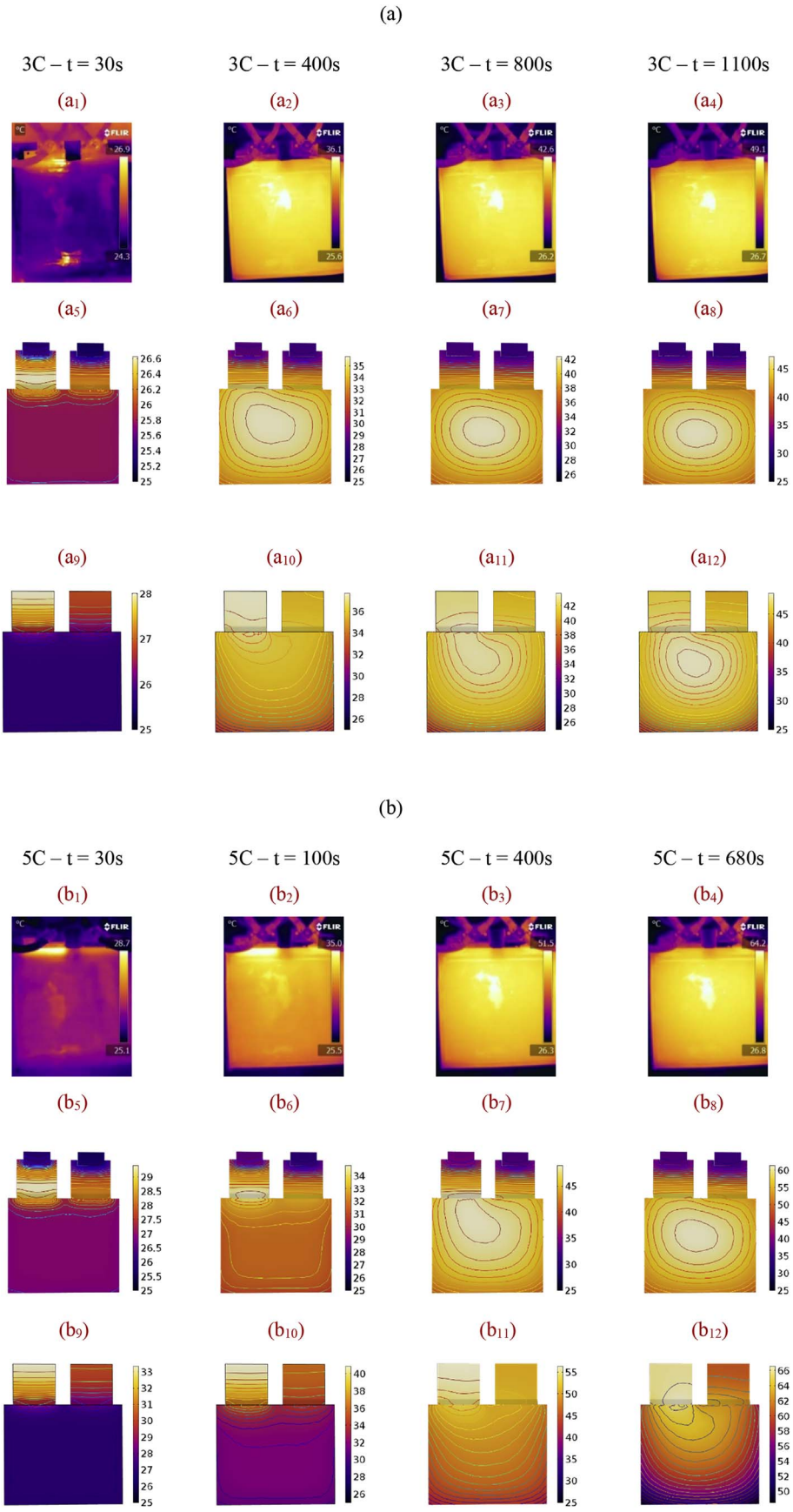

Fig. 7. Temperature evolution of the 53 Ah cell during a, (a) 3C discharge event and (b) 5C discharge event at 25°C. The first row, (a_1-a_4, b_1-b_4) shows the surface temperature of the cell obtained from the thermal camera, the second row, (a_5-a_8, b_5-b_8) is the simulation results with the same setup as the experiment. The simulation results at the third row, (a_9-a_{12}, b_9-b_{12}) are obtained by eliminating the brass connector, connecting the cells to the cycler.

is equal to 16.2, 9.5 and 7.4 °C. Similar to the race cycle the model prediction for 25°C and 45°C is accurate, but a larger deviation is observed at 5°C. The peak error for WLTP cycle at 5°C, 25°C and 45°C is equal to 12.1%, 5.3% and 2.7% versus an average error of 1.2%, 0.8% and 0.7% respectively. The error rises as the SOC decreases, especially for WLTP after 5000s where the SOC reduces to circa: 0.2. Knowing that a typical SOC range for EVs is between 0.2 and 0.8, to avoid overcharge or overdischarge [74], the peak error for (SOC < 0.2) can be eliminated. The accuracy of the current model is comparable to a recent study published by Farag et at. [28], covering a broad range of C-rates and temperatures.

6.3. Capacity and power

The capacity of the cell (obtained from the model and experiments) as a function of C-rate and ambient temperature is presented in Table 11. As seen, the model prediction for $T_{amb} > 15°C$ is fairly well with 4.8% error, whereas a larger error is observed at 5°C, equal to 12.3% at 0.5C. It is seen that the capacity increases as the temperature rises but its rate is not monotonic. Under 0.5C discharge, by increasing T_{amb} from 5°C to 45 °C the capacity increases by 20.6% while the increase rate is equal to 10.7% under 4C discharge event. In general, at low ambient temperatures the cell resistance is much higher and this leads to a lower power and capacity. However, due to the self-heating

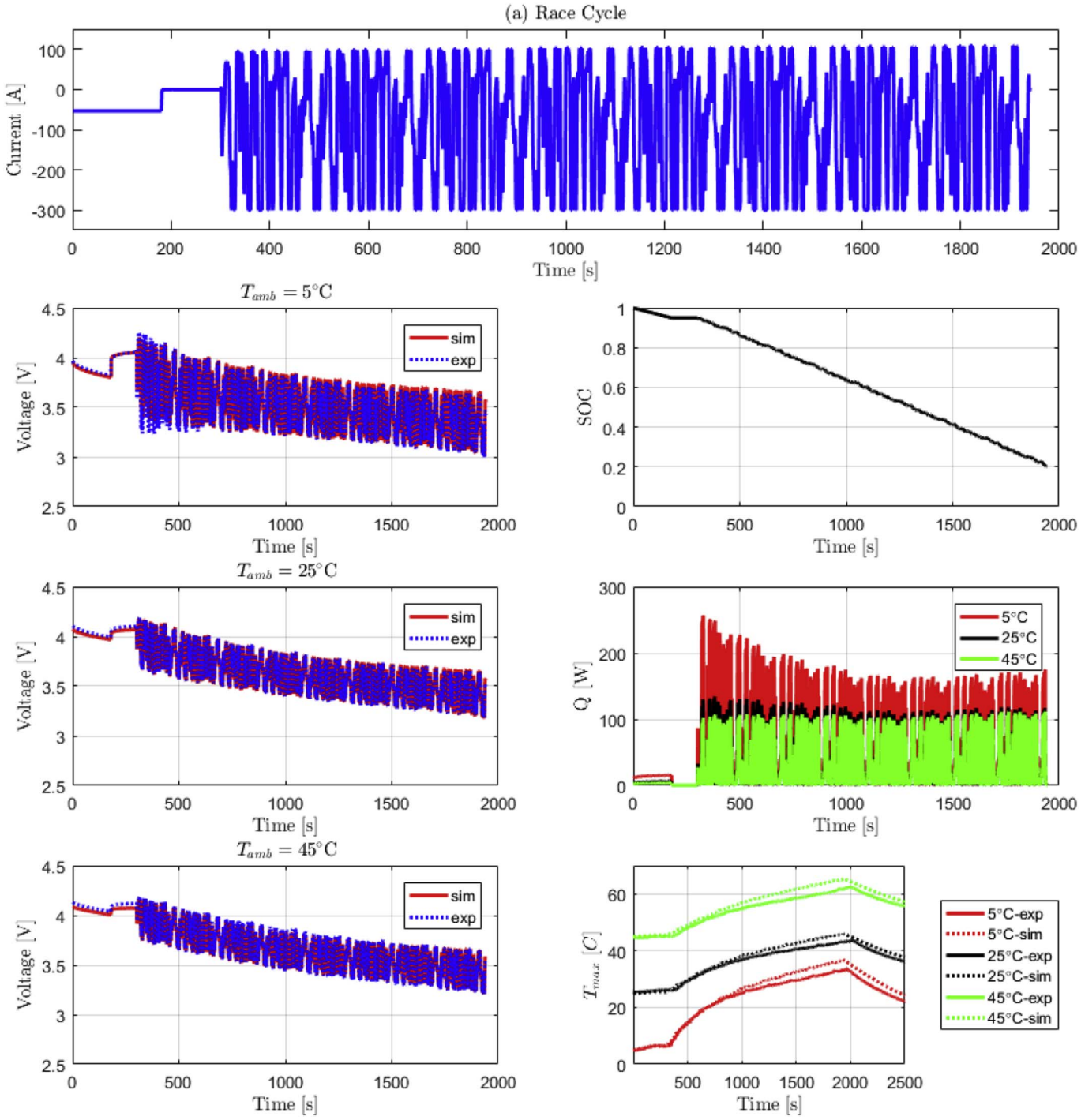

Fig. 8. Comparison between the experimental and the numerical terminal voltage corresponding to the 53 Ah cell under, (a) Race cycle, (b) WLTP class 3 cycle at 5°C, 25°C and 45°C.

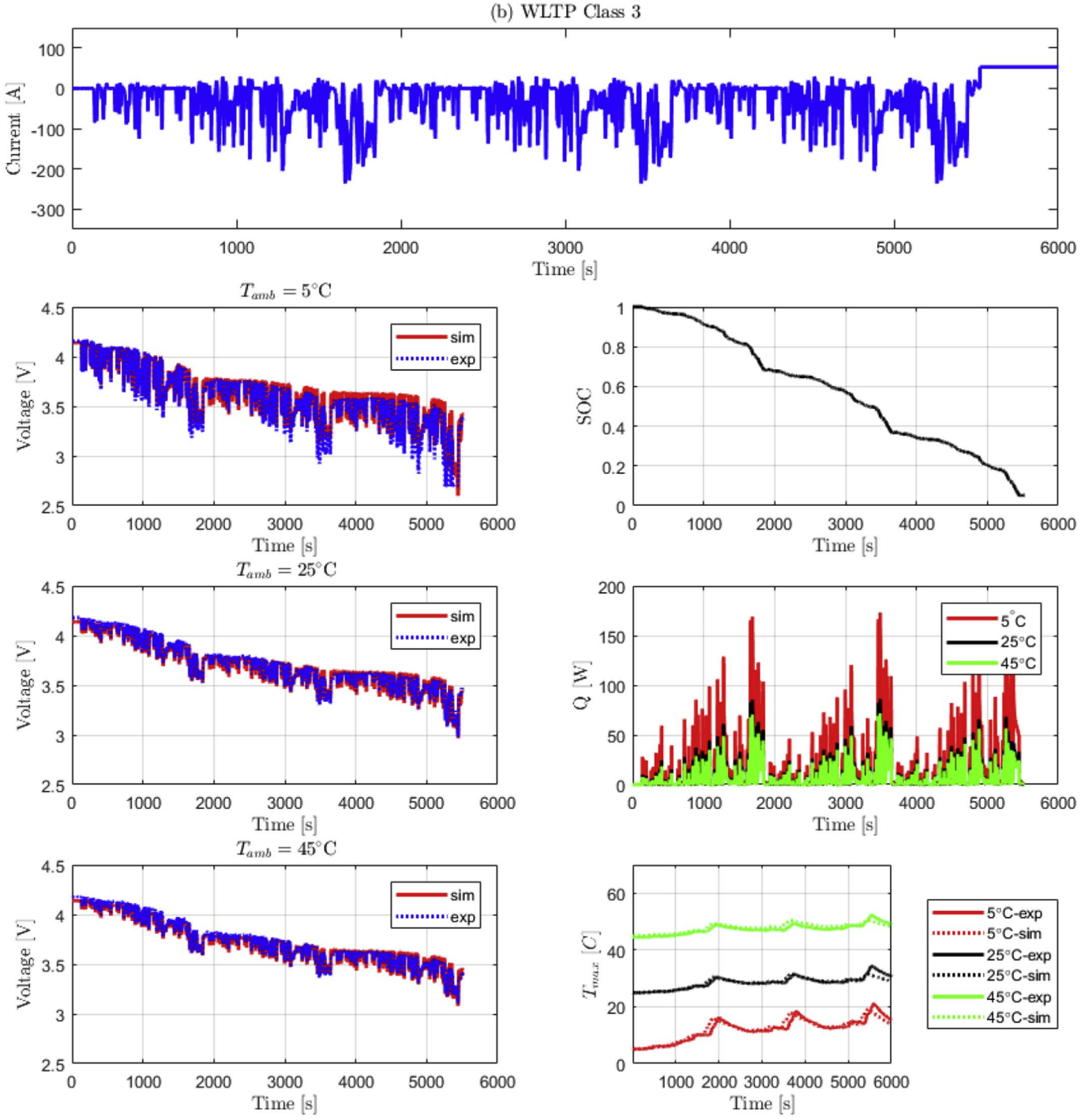

Fig. 8. (*continued*)

effect the capacity loss is less significant at higher C-rates, as seen in Fig. 5, and reported in Table 11.

The power output of the cells under continuous discharge conditions as well as duty cycles at different ambient temperatures are presented in Table 12. A maximum deviation of 6.3% is observed between the simulation and experimental data at 5°*C* ambient under 5C discharge rate. The results show that by decreasing the temperature from 45°*C* to 5°*C* the power loss is around 9.2% under 5C discharge and it becomes less significant as the current decreases, equal to 3.6% under 0.5C discharge. Moreover, the corresponding power loss is around 5.23% under the race cycle along with 7.57% under WLTP drive cycle.

7. Further work

The primary objective of this study was to present a systematic approach to fully parametrise and validate a large format cell and to introduce the full data set for it which has rarely been published within the literature. The underpinning methodology for experimental parameterisation, verification and model structure are deemed to be generic. However, the authors acknowledge that further research is required to quantify the performance of the cell model and its transferability to other cell chemistries and form factors. In this study the model is based on coupling of the 1D electrochemical and 1D thermal model to reduce the computational cost. Further the developed

Table 11
The capacity variation of the 53Ah cell over different C-rates and ambient temperatures. Sim corresponds to simulation results and exp represents the experimental data.

Capacity (Ah)		$T_{amb} = 5$°C	$T_{amb} = 15$°C	$T_{amb} = 25$°C	$T_{amb} = 35$°C	$T_{amb} = 45$°C
0.5C	sim	53.86	54.62	55.09	55.38	55.59
	exp	47.93	52.13	55.51	56.72	57.83
	error%	12.37	4.77	-0.76	-2.36	-0.04
1C	sim	52.88	53.84	54.49	54.90	55.19
	exp	47.49	51.30	54.66	56.24	57.71
	error%	11.35	4.95	-0.31	-2.38	-0.04
2C	sim	52.06	53.06	53.76	54.30	54.68
	exp	48.46	51.25	54.58	55.96	57.41
	error%	7.43	3.53	-1.50	-2.97	-0.05
3C	sim	51.72	52.65	53.39	53.93	54.33
	exp	49.44	51.71	54.89	56.07	57.06
	error%	4.61	1.82	-2.73	-3.82	-0.05
4C	sim	51.53	52.35	53.25	53.61	54.02
	exp	49.79	52.27	55.06	56.18	55.15
	error%	3.49	0.15	-3.28	-4.57	-0.02
5C	sim	51.38	52.19	52.92	53.37	53.81
	exp	49.57	52.90	55.18	55.71	
	error%	3.65	-1.34	-4.09	-4.20	

Peak Error: 0-2%	2-4%	4-6%	6-8%	8-10%	10-12%	12-14%

model is combined with a 3D thermal model sequentially to predict the temperature distribution in the cell scale. However, this assumption is valid as long as there is no active cooling in the system. It should be mentioned that to design a TMS, the two-way coupling between the 1D and 3D model is required, which will be considered in the future. The next stage of the research is to increase the accuracy of the model by OCV measurement of the single electrodes at different ambient temperatures rather than using literature data, along with introducing entropic terms of the individual electrodes instead of cell scale entropy measurement. This refinement will enable the model to predict the voltage and capacity of the cell more precisely, especially for low ambient temperatures. The second avenue of further study is to employ the now validated model for module and pack level research, by aggregating different cell models together to form a complete simulation of a battery assembly. As part of this work, a conceptual architecture of a battery pack design employing 53 Ah cells that has the equivalent electrical performance attributes to the TESLA S pack assembly is being designed. The impact of load imbalances within a parallel string on the temperature variation will be investigated and subsequently published. Moreover, novel thermal management systems will be introduced to the simulation in order to investigate different strategies to effectively remove the heat from such large format battery cells.

8. Conclusions

Using a P2D electrochemical approach coupled with a 1D and 3D lumped thermal model, this study presents a fully validated model of a large format 53 Ah for a wide range of continuous charge (0.5C-2C), discharge (0.5C-5C), and drive cycles (race cycle and WLTP class 3), under $5°C$–$45°C$ ambient temperature. Formulation of the model is

Table 12
The Power variation of the 53Ah cell over different C-rates and ambient temperatures. Sim corresponds to simulation results and exp represents the experimental data.

Power (W)		$T_{amb} = 5$°C	$T_{amb} = 15$°C	$T_{amb} = 25$°C	$T_{amb} = 35$°C	$T_{amb} = 45$°C
0.5C	sim	95.09	95.78	96.14	96.42	96.18
	exp	93.80	96.02	96.74	97.20	97.29
	error%	1.37	-0.25	-0.62	-0.80	-0.01
1C	sim	187.08	188.2	189.49	190.34	190.79
	exp	183.09	188.85	190.75	192.14	192.45
	error%	2.18	-0.34	-0.66	-0.94	0.01
2C	sim	364.93	368.74	371.41	373.51	375.66
	exp	354.42	368.17	372.42	376.33	377.17
	error%	2.96	0.15	-0.27	-0.74	0.00
3C	sim	538.37	543.56	548.76	552.43	555.00
	exp	517.85	540.48	546.69	553.72	555.18
	error%	3.96	0.57	0.38	-0.23	0.00
4C	sim	706.18	714.03	721.16	726.50	730.29
	exp	673.31	705.67	714.23	724.93	
	error%	4.88	1.18	0.97	0.22	
5C	sim	871.11	878.99	888.71	896.26	902.72
	exp	819.6	862.65	874.97		
	error%	4.88	1.18	0.97	0.22	
Race	sim	425.94		441.13		445.42
	exp	424.08		442.15		446.27
	error%	0.43		-0.23		0.00
WLTP	sim	124.12		130.15		131.31
	exp	122.72		130.69		132.01
	error%	1.14		-0.41		0.00

Peak Error: 0-1%	1-2%	2-3%	3-3-4%	4-5%

supported by a comprehensive set of experiments, for quantifying key parameters and for model validation. In addition, the full parameter-set for the model and the experimental methods employed, which are not normally included in the literature, are provided ensuring the model is a valuable resource to underpin further research.

Simulation results highlight that battery performance is highly dependent on ambient temperature. By decreasing the ambient temperature from 45°C to 5 °C the available capacity drops by 17.1% and 7.8% under 0.5C and 5C discharge respectively. Moreover, the corresponding power loss is found to be: 5.23% under the race cycle along with 7.57% under WLTP drive cycle. The increased internal resistance of the cell leads to 73% rise in heat generation under the race cycle along with a 119% increase under the WLTP duty cycle. Based on the results, one conclusion is that it is best to keep the operating temperature above 25°C as lower temperatures can lead to a considerable capacity loss, whilst for temperatures above 25°C the capacity gain is not significant. The upper limit for the temperature is defined by the aging rate and found to be around 35°C by a number of different researchers. Therefore, to keep a compromise between the battery performance and aging a temperature range of 25°C–35°C is recommended which is slightly different with the existing literature values, defined within a range of 15°C–35°C.

Overall, response dependency of lithium-ion battery to operating conditions underpins the value of the detailed performance of the cell under specific conditions. For example, safety and reliability of the cell can be improved, knowing how quickly the cell reaches to the cut-off temperature so that potential hazards such as thermal runaway can be avoided. Moreover, the existing correlation between the temperature and the achievable capacity, power and usable lifetime can help us extend the vehicle range and reduce the cost of the battery pack.

Acknowledgement

The research was undertaken as a part of ELEVATE project (EP/M009394/1) and the Energy Storage SuperGen (EP/L019469/1) both funded by the Engineering and Physical Science Research Council (EPSRC).

References

[1] M.A. Kiani, M.F. Mousavi, M.S. Rahmanifar, Synthesis of nano- and micro-particles of LiMn2O4: electrochemical investigation and assessment as a cathode in li battery, Int. J. Electrochem. Sci. 6 (2011) 2581–2595, http://dx.doi.org/10.1039/c1ee01598b.

[2] L.H. Saw, Y. Ye, A.A.O. Tay, W.T. Chong, S.H. Kuan, M.C. Yew, Computational fluid dynamic and thermal analysis of Lithium-ion battery pack with air cooling, Appl. Energy 177 (2016) 783–792, http://dx.doi.org/10.1016/j.apenergy.2016.05.122.

[3] T. Grandjean, A. Barai, E. Hosseinzadeh, Y. Guo, A. McGordon, J. Marco, Large format lithium ion pouch cell full thermal characterisation for improved electric vehicle thermal management, J. Power Sources 359 (2017) 215–225, http://dx.doi.org/10.1016/j.jpowsour.2017.05.016.

[4] H. Teng, K. Yeow, Design of Direct and Indirect Liquid Cooling Systems for High-Capacity, High-Power Lithium-Ion Battery Packs, SAE Technical Paper 2012-01-2017 (2012), http://dx.doi.org/10.4271/2012-01-2017 doi:10.4271/2012-01-2017.

[5] T.R. Tanim, C.D. Rahn, C.-Y. Wang, A temperature dependent, single particle, lithium ion cell model including electrolyte diffusion, J. Dyn. Syst. Meas. Contr. 137 (2014) 011005, , http://dx.doi.org/10.1115/1.4028154.

[6] Q. Wang, B. Jiang, B. Li, Y. Yan, A critical review of thermal management models and solutions of lithium-ion batteries for the development of pure electric vehicles, 64 (2016) 106–128, http://dx.doi.org/10.1016/j.rser.2016.05.033.

[7] R.E. Gerver, 3D Thermal-Electrochemical Lithium-Ion Battery Computational Modeling, Engineering, (2009).

[8] Y. Ji, Y. Zhang, C.-Y. Wang, Li-ion cell operation at low temperatures, J. Electrochem. Soc. 160 (2013) A636–A649, http://dx.doi.org/10.1149/2.047304jes.

[9] Y. Ye, Y. Shi, L. Huat, A.A.O. Tay, Performance assessment and optimization of a heat pipe thermal management system for fast charging lithium ion battery packs, Int. J. Heat Mass Tran. 92 (2016) 893–903, http://dx.doi.org/10.1016/j.ijheatmasstransfer.2015.09.052.

[10] Y. Troxler, B. Wu, M. Marinescu, V. Yufit, Y. Patel, A.J. Marquis, N.P. Brandon, G.J. Offer, The effect of thermal gradients on the performance of lithium-ion batteries, J. Power Sources 247 (2014) 1018–1025, http://dx.doi.org/10.1016/j.jpowsour.2013.06.084.

[11] U.S. Kim, C.B. Shin, C.S. Kim, Effect of electrode configuration on the thermal behavior of a lithium-polymer battery, J. Power Sources 180 (2008) 909–916, http://dx.doi.org/10.1016/j.jpowsour.2007.09.054.

[12] P. Taheri, A. Mansouri, B. Schweitzer, M. Yazdanpour, M. Bahrami, Electrical constriction resistance in current collectors of large-scale lithium-ion batteries, J. Electrochem. Soc. 160 (2013) A1731–A1740, http://dx.doi.org/10.1149/2.041310jes.

[13] U.S. Kim, J. Yi, C.B. Shin, T. Han, S. Park, Modelling the thermal behaviour of a lithium-ion battery during charge, J. Power Sources 196 (2011) 5115–5121, http://dx.doi.org/10.1016/j.jpowsour.2011.01.103.

[14] P. Taheri, A. Mansouri, M. Yazdanpour, M. Bahrami, Theoretical analysis of potential and current distributions in planar electrodes of lithium-ion batteries, Electrochim. Acta 133 (2014) 197–208, http://dx.doi.org/10.1016/j.electacta.2014.04.040.

[15] B. Wu, Z. Li, J. Zhang, Thermal design for the pouch-type large-format lithium-ion batteries: I. Thermo-electrical modeling and origins of temperature non-uniformity, J. Electrochem. Soc. 162 (2014) A181–A191, http://dx.doi.org/10.1149/2.0831501jes.

[16] A. Samba, N. Omar, H. Gualous, Y. Firouz, P. Van Den Bossche, J. Van Mierlo, T.I. Boubekeur, Development of an advanced two-dimensional thermal model for large size lithium-ion pouch cells, Electrochim. Acta 117 (2014) 246–254, http://dx.doi.org/10.1016/j.electacta.2013.11.113.

[17] K. Murashko, J. Pyrhonen, L. Laurila, Three-dimensional thermal model of a lithium ion battery for hybrid mobile working machines: determination of the model parameters in a pouch cell, IEEE Trans. Energy Convers. 28 (2013) 335–343, http://dx.doi.org/10.1109/TEC.2013.2255291.

[18] S.J. Bazinski, X. Wang, Predicting heat generation in a lithium-ion pouch cell through thermography and the lumped capacitance model, J. Power Sources 305 (2016) 97–105, http://dx.doi.org/10.1016/j.jpowsour.2015.11.083.

[19] S. Wijewardana, R. Vepa, M.H. Shaheed, Dynamic battery cell model and state of charge estimation, J. Power Sources 308 (2016) 109–120, http://dx.doi.org/10.1016/j.jpowsour.2016.01.072.

[20] T. Yuksel, S. Litster, V. Viswanathan, J.J. Michalek, Plug-in hybrid electric vehicle LiFePO4 battery life implications of thermal management, driving conditions, and regional climate, J. Power Sources 338 (2017) 49–64, http://dx.doi.org/10.1016/j.jpowsour.2016.10.104.

[21] M. Xu, Z. Zhang, X. Wang, L. Jia, L. Yang, Two-dimensional electrochemical-thermal coupled modeling of cylindrical LiFePO4 batteries, J. Power Sources 256 (2014) 233–243, http://dx.doi.org/10.1016/j.jpowsour.2014.01.070.

[22] J. Li, Y. Cheng, L. Ai, M. Jia, S. Du, B. Yin, S. Woo, H. Zhang, 3D simulation on the internal distributed properties of lithium-ion battery with planar tabbed configuration, J. Power Sources 293 (2015) 993–1005, http://dx.doi.org/10.1016/j.jpowsour.2015.06.034.

[23] M. Xiao, S.-Y. Choe, Dynamic modeling and analysis of a pouch type LiMn2O4/Carbon high power Li-polymer battery based on electrochemical-thermal principles, J. Power Sources 218 (2012) 357–367, http://dx.doi.org/10.1016/j.jpowsour.2012.05.103.

[24] M. Xiao, S.Y. Choe, Theoretical and experimental analysis of heat generations of a pouch type LiMn2O4/carbon high power Li-polymer battery, J. Power Sources 241 (2013) 46–55, http://dx.doi.org/10.1016/j.jpowsour.2013.04.062.

[25] A. Samba, N. Omar, H. Gualous, O. Capron, P. Van Den Bossche, J. Van Mierlo, Impact of tab location on large format lithium-ion pouch cell based on fully coupled tree-dimensional electrochemical-thermal modeling, Electrochim. Acta 147 (2014) 319–329, http://dx.doi.org/10.1016/j.electacta.2014.08.115.

[26] K. Smith, C.-Y. Wang, Power and thermal characterization of a lithium-ion battery pack for hybrid-electric vehicles, J. Power Sources 160 (2006) 662–673, http://dx.doi.org/10.1016/j.jpowsour.2006.01.038.

[27] B. Wu, V. Yufit, M. Marinescu, G.J. Offer, R.F. Martinez-Botas, N.P. Brandon, Coupled thermal-electrochemical modelling of uneven heat generation in lithium-ion battery packs, J. Power Sources 243 (2013) 544–554, http://dx.doi.org/10.1016/j.jpowsour.2013.05.164.

[28] M. Farag, H. Sweity, M. Fleckenstein, S. Habibi, Combined electrochemical, heat generation, and thermal model for large prismatic lithium-ion batteries in real-time applications, J. Power Sources 360 (2017) 618–633, http://dx.doi.org/10.1016/j.jpowsour.2017.06.031.

[29] I.A. Hunt, Y. Zhao, Y. Patel, J. Offer, Surface cooling causes accelerated degradation compared to tab cooling for lithium-ion pouch cells, J. Electrochem. Soc. 163 (2016) A1846–A1852, http://dx.doi.org/10.1149/2.0361609jes.

[30] E. Hosseinzadeh, A. Barai, J. Marco, P. Jennings, A Comparative Study on Different Cooling Strategies for Lithium-Ion Battery Cells, The European Battery, Hybrid and Fuel Cell Electric Vehicle Congress (EEVC 2017), (2017), pp. 1–9.

[31] Current density and state of charge inhomogeneities in Li-ion battery cells with LiFePO4 as cathode material due to temperature gradients, J. Power Sources 196 (2011) 4769–4778, http://dx.doi.org/10.1016/J.JPOWSOUR.2011.01.043.

[32] E. Schuster, C. Ziebert, A. Melcher, M. Rohde, H.J. Seifert, Thermal behavior and electrochemical heat generation in a commercial 40 Ah lithium ion pouch cell, J. Power Sources 286 (2015) 580–589, http://dx.doi.org/10.1016/j.jpowsour.2015.03.170.

[33] V. Ramadesigan, P.W.C. Northrop, S. De, S. Santhanagopalan, R.D. Braatz, V.R. Subramanian, Modeling and simulation of lithium-ion batteries from a systems engineering perspective, J. Electrochem. Soc. 159 (2012) R31–R45, http://dx.doi.org/10.1149/2.018203jes.

[34] A.M. Bizeray, S. Zhao, S.R. Duncan, D.A. Howey, Lithium-ion battery thermal-electrochemical model-based state estimation using orthogonal collocation and a modified extended Kalman filter, J. Power Sources 296 (2015) 400–412, http://dx.

doi.org/10.1016/j.jpowsour.2015.07.019.
[35] E. Hosseinzadeh, J. Marco, P. Jennings, Electrochemical-thermal modelling and optimisation of lithium-ion battery design parameters using analysis of variance, Energies 10 (2017) 1278, http://dx.doi.org/10.3390/en10091278.
[36] D. Worwood, Q. Kellner, M. Wojtala, W.D. Widanage, R. McGlen, D. Greenwood, J. Marco, A new approach to the internal thermal management of cylindrical battery cells for automotive applications, J. Power Sources 346 (2017) 151–166, http://dx.doi.org/10.1016/j.jpowsour.2017.02.023.
[37] D. Worwood, E. Hosseinzadeh, K.Q.J. Marco, D. Greenwood, M.R.W. Widanage, A. Barai, P. Jennings, Thermal analysis of a lithium-ion pouch cell under aggressive automotive duty cycles with minimal cooling, IET Hybrid and Electric Vehicles Conference (HEVC 2016), 2016, pp. 2–3.
[38] C. Forgez, D. Vinh, G. Friedrich, M. Morcrette, C. Delacourt, Thermal modeling of a cylindrical LiFePO 4/graphite lithium-ion battery, 195 (2010) 2961–2968, http://dx.doi.org/10.1016/j.jpowsour.2009.10.105.
[39] A Homogenized Thermal Model For Lithium Ion Batteries Erlend Finden, (n.d).
[40] K.E. Thomas, J. Newman, Thermal Modeling of Porous Insertion Electrodes, (2003), pp. 176–192, http://dx.doi.org/10.1149/1.1531194.
[41] C. Heubner, M. Schneider, A. Michaelis, Detailed study of heat generation in porous LiCoO2 electrodes, J. Power Sources 307 (2016) 199–207, http://dx.doi.org/10.1016/j.jpowsour.2015.12.096.
[42] V.V. Viswanathan, D. Choi, D. Wang, W. Xu, S. Towne, R.E. Williford, J.G. Zhang, J. Liu, Z. Yang, Effect of entropy change of lithium intercalation in cathodes and anodes on Li-ion battery thermal management, J. Power Sources 195 (2010) 3720–3729, http://dx.doi.org/10.1016/j.jpowsour.2009.11.103.
[43] K. Jalkanen, T. Aho, K. Vuorilehto, Entropy change effects on the thermal behavior of a LiFePO4/graphite lithium-ion cell at different states of charge, J. Power Sources 243 (2013) 354–360, http://dx.doi.org/10.1016/j.jpowsour.2013.05.199.
[44] N.S. Hudak, L.E. Davis, G. Nagasubramanian, Cycling-induced changes in the entropy profiles of lithium cobalt oxide electrodes, J. Electrochem. Soc. 162 (2014) A315–A321, http://dx.doi.org/10.1149/2.0071503jes.
[45] F. Jiang, P. Peng, Y. Sun, Thermal analyses of LiFePO4/graphite battery discharge processes, J. Power Sources 243 (2013) 181–194, http://dx.doi.org/10.1016/j.jpowsour.2013.05.089.
[46] M. Xiao, S.Y. Choe, Theoretical and experimental analysis of heat generations of a pouch type LiMn2O4/carbon high power Li-polymer battery, J. Power Sources 241 (2013) 46–55, http://dx.doi.org/10.1016/j.jpowsour.2013.04.062.
[47] J. Yi, U.S. Kim, C.B. Shin, T. Han, S. Park, Three-Dimensional thermal modeling of a lithium-ion battery considering the combined effects of the electrical and thermal contact resistances between current collecting tab and lead wire, J. Electrochem. Soc. 160 (2013) A437–A443, http://dx.doi.org/10.1149/2.039303jes.
[48] Á.G. Miranda, C.W. Hong, Integrated modeling for the cyclic behavior of high power Li-ion batteries under extended operating conditions, Appl. Energy 111 (2013) 681–689, http://dx.doi.org/10.1016/j.apenergy.2013.05.047.
[49] J. Yi, U.S. Kim, C.B. Shin, T. Han, S. Park, Three-Dimensional thermal modeling of a lithium-ion battery considering the combined effects of the electrical and thermal contact resistances between current collecting tab and lead wire, J. Electrochem. Soc. 160 (2013) A437–A443, http://dx.doi.org/10.1149/2.039303jes.
[50] G. Vertiz, M. Oyarbide, H. Macicior, O. Miguel, I. Cantero, P. Fernandez De Arroiabe, I. Ulacia, Thermal characterization of large size lithium-ion pouch cell based on 1d electro-thermal model, J. Power Sources 272 (2014) 476–484, http://dx.doi.org/10.1016/j.jpowsour.2014.08.092.
[51] A. Tourani, P. White, P. Ivey, Analysis of electric and thermal behaviour of lithium-ion cells in realistic driving cycles, J. Power Sources 268 (2014) 301–314, http://dx.doi.org/10.1016/j.jpowsour.2014.06.010.
[52] S.C. Chen, C.C. Wan, Y.Y. Wang, Thermal analysis of lithium-ion batteries, J. Power Sources 140 (2005) 111–124, http://dx.doi.org/10.1016/j.jpowsour.2004.05.064.
[53] Y. Ma, H. Teng, M. Thelliez, Electro-thermal modeling of a lithium-ion battery system, 3 (2016) 306–317.
[54] S.J. Drake, D.A. Wetz, J.K. Ostanek, S.P. Miller, J.M. Heinzel, A. Jain, Measurement of anisotropic thermophysical properties of cylindrical Li-ion cells, J. Power Sources 252 (2014) 298–304, http://dx.doi.org/10.1016/j.jpowsour.2013.11.107.
[55] K. Shah, C. McKee, D. Chalise, A. Jain, Experimental and numerical investigation of core cooling of Li-ion cells using heat pipes, Energy 113 (2016) 852–860, http://dx.doi.org/10.1016/j.energy.2016.07.076.
[56] Y. Ye, L.H. Saw, Y. Shi, K. Somasundaram, A.A.O. Tay, Effect of thermal contact resistances on fast charging of large format lithium ion batteries, Electrochim. Acta 134 (2014) 327–337, http://dx.doi.org/10.1016/j.electacta.2014.04.134.
[57] J. Li, Y. Cheng, M. Jia, Y. Tang, Y. Lin, Z. Zhang, Y. Liu, An electrochemical-thermal model based on dynamic responses for lithium iron phosphate battery, J. Power Sources 255 (2014) 130–143, http://dx.doi.org/10.1016/j.jpowsour.2014.01.007.
[58] P. Amiribavandpour, W. Shen, D. Mu, A. Kapoor, An improved theoretical electrochemical-thermal modelling of lithium-ion battery packs in electric vehicles, J. Power Sources 284 (2015) 328–338, http://dx.doi.org/10.1016/j.jpowsour.2015.03.022.
[59] W. Wu, X. Xiao, X. Huang, The effect of battery design parameters on heat generation and utilization in a Li-ion cell, Electrochim. Acta 83 (2012) 227–240, http://dx.doi.org/10.1016/j.electacta.2012.07.081.
[60] T.M. Bandhauer, S. Garimella, T.F. Fuller, Temperature-dependent electrochemical heat generation in a commercial lithium-ion battery, J. Power Sources 247 (2014) 618–628, http://dx.doi.org/10.1016/j.jpowsour.2013.08.015.
[61] S.B.D. Stewart, P.D. Albertus, V.D.D. Srinivasan, I. Plitz, N.D.D. Pereira, G.D.D. Amatucci, J.D.B.D. Newman, Optimizing the performance of lithium titanate spinel paired with activated carbon or iron phosphate, J. Electrochem. Soc. 155 (2008) A253–A261, http://dx.doi.org/10.1149/1.2830552.
[62] L. Zhang, C. Lyu, G. Hinds, L. Wang, W. Luo, J. Zheng, K. Ma, Parameter sensitivity analysis of cylindrical LiFePO4 battery performance using multi-physics modeling, J. Electrochem. Soc. 161 (2014) A762–A776, http://dx.doi.org/10.1149/2.048405jes.
[63] T.R. Tanim, C.D. Rahn, C.-Y. Wang, A temperature dependent, single particle, lithium ion cell model including electrolyte diffusion, J. Dyn. Syst. Meas. Contr. 137 (2014) 011005, , http://dx.doi.org/10.1115/1.4028154.
[64] W. Du, A. Gupta, X. Zhang, A.M. Sastry, W. Shyy, Effect of cycling rate, particle size and transport properties on lithium-ion cathode performance, Int. J. Heat Mass Tran. 53 (2010) 3552–3561, http://dx.doi.org/10.1016/j.ijheatmasstransfer.2010.04.017.
[65] K.A. Smith, C. Wang, by, (2006).
[66] A. Barai, G.H. Chouchelamane, Y. Guo, A. McGordon, P. Jennings, A study on the impact of lithium-ion cell relaxation on electrochemical impedance spectroscopy, J. Power Sources 280 (2015) 74–80, http://dx.doi.org/10.1016/j.jpowsour.2015.01.097.
[67] W.S. Zhang, Construction, calibration and testing of a decimeter-size heat-flow calorimeter, Thermochim. Acta 499 (2010) 128–132, http://dx.doi.org/10.1016/j.tca.2009.11.013.
[68] S. Chacko, Y.M. Chung, Thermal modelling of Li-ion polymer battery for electric vehicle drive cycles, J. Power Sources 213 (2012) 296–303, http://dx.doi.org/10.1016/j.jpowsour.2012.04.015.
[69] W. Tong, K. Somasundaram, E. Birgersson, A.S. Mujumdar, C. Yap, Numerical investigation of water cooling for a lithium-ion bipolar battery pack, Int. J. Therm. Sci. 94 (2015) 259–269, http://dx.doi.org/10.1016/j.ijthermalsci.2015.03.005.
[70] H.H. Huang, H.Y. Chen, K.C. Liao, H.T. Young, C.F. Lee, J.Y. Tien, Thermal-electrochemical coupled simulations for cell-to-cell imbalances in lithium-iron-phosphate based battery packs, Appl. Therm. Eng. 123 (2017) 584–591, http://dx.doi.org/10.1016/j.applthermaleng.2017.05.105.
[71] U. Seong Kim, J. Yi, C.B. Shin, T. Han, S. Park, Modeling the dependence of the discharge behavior of a lithium-ion battery on the environmental temperature, J. Electrochem. Soc. 158 (2011) A611, , http://dx.doi.org/10.1149/1.3565179.
[72] C. Veth, D. Dragicevic, C. Merten, Thermal characterizations of a large-format lithium ion cell focused on high current discharges, J. Power Sources 267 (2014) 760–769, http://dx.doi.org/10.1016/j.jpowsour.2014.05.139.
[73] L. Su, J. Zhang, C. Wang, Y. Zhang, Z. Li, Y. Song, T. Jin, Z. Ma, Identifying main factors of capacity fading in lithium ion cells using orthogonal design of experiments, Appl. Energy 163 (2016) 201–210, http://dx.doi.org/10.1016/j.apenergy.2015.11.014.
[74] R.F. Nelson, Power requirements for batteries in hybrid electric vehicles, J. Power Sources 91 (2000) 2–26, http://dx.doi.org/10.1016/S0378-7753(00)00483-3.